

CLC _____

Number _____

UDC _____

Available for reference ☐ Yes ☐ No



Undergraduate Thesis

Thesis Title: _____
Integration of SAW Sensing and

RFID Communications

Student Name: _____
Tianyang Chen

Student ID: _____
12111524

Department: _____
Electronic & Electrical Engineering

Program: _____
Undergraduate

Thesis Advisor: _____
Tao Ye

Date: 06 May 2025

COMMITMENT OF HONESTY

1. I solemnly promise that the paper presented comes from my independent research work under my supervisor's supervision. All statistics and images are real and reliable.

2. Except for the annotated reference, the paper contains no other published work or achievement by person or group. All people making important contributions to the study of the paper have been indicated clearly in the paper.

3. I promise that I did not plagiarize other people's research achievement or forge related data in the process of designing topic and research content.

4. If there is violation of any intellectual property right, I will take legal responsibility myself.

Signature:



Date:

06 May 2025

[ABSTRACT]: This thesis explores two synergistic advancements in passive wireless sensing for wearable applications. First, we develop a textile-integrated radio frequency identification (RFID) tag by embedding commercial RFID chips into flexible conductive yarns, forming fiber-like structures that can be seamlessly embroidered into fabrics. By optimizing antenna geometries and systematically evaluating stitching patterns, we demonstrate how textile-compatible layouts enhance mechanical stability and radiation efficiency compared to rigid planar designs. This innovation enables unobtrusive epidermal integration of RFID sensing for body-worn applications. Second, to augment conventional RFID sensing, we design lithium niobate-based surface acoustic wave (SAW) resonators with temperature-dependent frequency responses. A software-defined radio (SDR) reader architecture is proposed to decode both RFID identity codes and SAW sensor signatures via shared backscatter modulation, theoretically enabling co-sensing within a unified protocol framework. The full hardware integration is ongoing, these dual contributions—textile-optimized RFID morphology and SAW-augmented sensing principles—collectively establish a foundation for passive integrated sensing and communication (ISAC) systems. The fiber-based RFID platform addresses wearability constraints, while the hybrid SAW-RFID paradigm extends passive sensing beyond motion detection. Future work will unify these components into a body area network (BAN), leveraging piezoelectric functionalization for multimodal biosensing.

[Keywords]: RFID; SAW; ISAC; Wearable Electronics; Passive Backscatter Communication

结合射频识别的声表面波无线传感系统

陈天阳

(电子与电气工程系 指导教师：叶 涛)

[摘要]：该文基于结合射频识别（RFID）的声表面波（SAW）可穿戴无源无线传感展开研究。首先，研究设计了集成于织物的 RFID 标签，将商用 RFID 芯片嵌入柔性导电纱线中，实现了 RFID 与织物的深度集成。研究优化了天线结构，实现的可穿戴标签机械及辐射性能优于传统设计。其次，为实现增强的 RFID 通信感知一体化（ISAC），研究设计了一种 SAW 谐振器，其工作频率对温度具有敏感性。进一步，研究提出了一种基于软件定义无线电（SDR）的读取器架构，基于无源反射式通信同时获取 RFID 识别码及 SAW 传感特征信号，致力于实现统一通信协议框架下的 ISAC。研究将要完善的织物 RFID 与 SAW 的集成面向实现无源 ISAC——织物 RFID 将提升穿戴舒适性，而 SAW 的增强可将无源传感推广至更多参数。后续研究将进一步构建人体局域网（BAN），基于压电功能性实现多模态生物传感。

[关键词]：射频识别技术；声表面波；通信感知一体化；可穿戴设备；无源反射式通信

Contents

| | | |
|----------|--|-----------|
| 1 | Introduction | 1 |
| 1.1 | Background | 1 |
| 1.1.1 | Radio Frequency Identification (RFID)..... | 1 |
| 1.1.2 | Surface Acoustic Wave (SAW) | 5 |
| 1.2 | Related Works | 7 |
| 1.2.1 | RFID Tags and Readers | 7 |
| 1.2.2 | SAW Devices | 17 |
| 1.3 | This Work | 20 |
| 2 | RFID Tags | 21 |
| 2.1 | Integration of RFID Chip and Wearable Radiating Element..... | 22 |
| 2.1.1 | Selection of Chip and Radiator | 22 |
| 2.1.2 | Integration Process..... | 24 |
| 2.1.3 | Encapsulation and Textile Integration..... | 25 |
| 2.2 | Wearable RFID Antenna Design | 27 |
| 2.2.1 | Dipole..... | 27 |
| 2.2.2 | Meanderline | 31 |
| 2.2.3 | Inductive Loop..... | 33 |
| 2.3 | Wearable RFID Tag Evaluation..... | 34 |
| 2.3.1 | Tag Prototypes | 34 |

| | | |
|----------|---------------------------------------|-----------|
| 2.3.2 | Testing Platform..... | 35 |
| 2.3.3 | Reading Performance..... | 36 |
| 3 | SAW-RFID System | 39 |
| 3.1 | Principles of SAW | 39 |
| 3.1.1 | Rayleigh Waves..... | 39 |
| 3.1.2 | Interdigital Transducer (IDT)..... | 40 |
| 3.2 | SAW Fabrication | 41 |
| 3.2.1 | Piezoelectric Materials..... | 41 |
| 3.2.2 | IDT Structure | 41 |
| 3.2.3 | Fabrication Process | 42 |
| 3.3 | SAW Characterization | 44 |
| 3.3.1 | Characterization Setup..... | 44 |
| 3.3.2 | Resonance Measurement | 44 |
| 3.3.3 | Sensing Response..... | 45 |
| 3.4 | Interrogation Principals | 46 |
| 3.4.1 | Interrogation of SAW | 46 |
| 3.4.2 | Interrogation of RFID | 51 |
| 3.4.3 | Towards an RFID-SAW ISAC Scheme | 54 |
| 3.5 | RFID-SAW Reading Framework | 55 |
| 3.5.1 | NI-LabVIEW Based SDR with FMCW | 55 |
| 3.5.2 | Limitations | 58 |

| | | |
|----------|-------------------------------------|-----------|
| 3.5.3 | GNU Radio Based SDR with OFDM | 59 |
| 3.5.4 | Optimizations..... | 62 |
| 4 | Conclusion..... | 66 |
| 4.1 | Summary | 66 |
| 4.2 | Outlook..... | 66 |
| | Reference | 68 |

1 Introduction

1.1 Background

1.1.1 Radio Frequency Identification (RFID)

Radio Frequency Identification (RFID) is a non-contact identification technology that enables data exchange between a reader and an electronic tag via radio waves[1], thereby facilitating the identification and tracking of target objects. Specifically, RFID technology operates based on backscatter communication, whereby the reader emits a continuous wave signal, and the tag reflects a modulated version of this signal—via load modulation or harmonic reflection—to transmit data back to the reader[1].

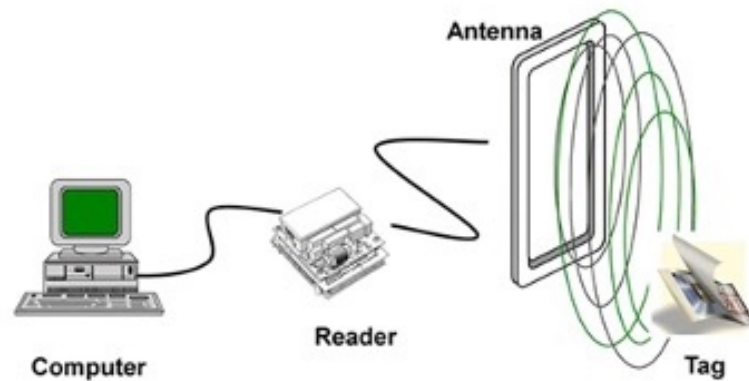


Fig 1-1 An RFID System

An RFID system, as shown in Fig 1-1, typically consists of three components[3]: tags, readers, and a control system (e.g., a computer). Tags can be classified as passive (powered by the electromagnetic field from the reader) or active (equipped with an internal battery). Based on the operating frequency, RFID systems are further categorized into low-frequency (LF, 30–300 kHz), high-frequency (HF, 3–30 MHz), ultra-high-frequency (UHF, 300 MHz–3 GHz), and microwave frequency bands (above 3 GHz)[3]. Each frequency band offers distinct communication ranges and application scenarios.

The conceptual origin of RFID dates back to World War II, when the Allies employed Identification Friend or Foe (IFF) systems that relied on radar signal

reflections to distinguish friendly aircraft. These early RFID systems were extremely simple, conveying only binary presence information[1]. In 1948, H. Stockman formally introduced the principle of communication by means of reflected power in his seminal work *Communication by Means of Reflected Power*, significantly advancing the foundational theory of RFID[1]. In 1955, J. H. Richmond and colleagues first applied load modulation in the RFID domain, paving the way for applications in biomedical near-field imaging and measurement[3].

During the 1960s and 1970s, RFID experienced rapid development. Numerous patents and theoretical advancements emerged. In 1960, D. B. Harris proposed an RF transmission system based on a modulated passive responder[1]. Subsequently, in 1968, J. H. Vogelmann designed a radar-backscatter-based passive data transmission technique. Meanwhile, R. H. Harrington's electromagnetic theory of loaded scatterers, established in 1964, provided a rigorous theoretical framework for RFID[1]. The advent of integrated circuits further enabled storage of multiple bits of information on tags, thus propelling RFID toward practical implementation. Notably, a large-scale application emerged in 1975 when Los Alamos National Laboratory developed a system for monitoring animal body temperature[3]. Applications in merchandise tracking, theft prevention, and automated toll collection systems like the U.S. E-ZPass, as shown in Fig 1-2, which further accelerated the adoption of RFID[1][3].



Fig 1-2 E-ZPass used by the Author during a Self-drive Campus Tour

From the 1980s onward, RFID technology entered a phase of standardization and widespread commercial deployment. International standards, such as those established by EPCglobal and the Electronic Product Code (EPC) framework, have enabled large-

scale implementation of RFID in logistics and supply chain management[1]. With the advancement of 5G networks and the rise of the industry 4.0 paradigm, the integration of RFID and the Internet of Things (IoT) has become increasingly prominent[1]. In recent years, RFID has also evolved rapidly in the field of wireless sensing, leveraging its non-contact and non-invasive characteristics in applications such as environmental monitoring, food safety, healthcare, and smart agriculture. According to IDTechEx 2022 report, the global RFID market reached \$11.6 billion in 2021 and is expected to maintain steady growth[1], highlighting its broad potential for future applications.



Fig 1-3 NFC System

A particularly well-known derivative of RFID is Near Field Communication (NFC), which as shown in Fig 1-3, offers short-range, high-security wireless communication. NFC was co-developed by Sony and Philips in 2002, and its standardization was promoted by the establishment of the NFC Forum in 2004[3]. With the widespread adoption of smartphones, NFC has become integral to daily life scenarios such as mobile payments, access control, and smart interactions. Owing to its security and convenience, NFC has become an indispensable component of modern life and the IoT ecosystem.

In recent years, RFID has become a cornerstone of wireless sensing systems due to its non-contact, battery-less, and non-invasive properties[5]. Without requiring external power, RFID tags can engage in backscatter-based communication with readers, enabling simultaneous identification and sensing. These characteristics—low power consumption and high integrability—have led to widespread adoption in domains such as smart homes, industrial automation, healthcare, and environmental monitoring. As

Industry 4.0, the Internet of Things (IoT), and 5G communication rapidly evolve, the complexity of sensing scenarios and the demand for multidimensional data acquisition have significantly increased. According to market research, the global RFID market reached \$11.6 billion in 2021 and is projected to exceed 13 billion by 2023, underscoring its growing importance[1].

From the wireless communication perspective, the concept of ISAC has gained traction in response to the growing need for sensing capabilities in next-generation systems. In passive backscatter communication scenarios, UHF RFID is emerging as an ideal platform for realizing Passive ISAC due to its low-power and long-range communication capabilities[10]. Current passive sensing methods based on UHF RFID primarily rely on mechanical deformation of the tag antenna (e.g., stretching or bending) or changes in the dielectric environment surrounding the tag. These environmental changes are inferred through variations in backscattered signal parameters such as RSSI and phase shift, enabling indirect sensing of temperature, humidity, strain, and other physical quantities.

From a system design perspective, RFID-based sensing can be categorized into two main approaches: response-based sensing and data-encoded sensing. Response-based sensing refers to detecting changes in the tag's response signal to indirectly infer variations in environmental parameters. This is typically achieved through impedance modulation of the antenna induced by the sensed variable. For example, when a fabric-integrated antenna deforms, its input impedance changes, causing mismatch with the RFID chip[5]. This impedance mismatch leads to detectable variations in RSSI or phase, which are used for sensing. However, the reliability of this method is heavily dependent on the spatial configuration and multipath conditions between the tag and the reader, limiting its robustness and repeatability.

In contrast, data-encoded sensing directly writes the output of an external sensor into the non-volatile memory of the RFID chip via a serial interface (e.g., SPI), and this information is subsequently read by the reader alongside the tag's ID. A representative example is the EM4325 chip, which supports SPI-based data writing and reading in a

fully passive mode. This approach offers better path invariance and stronger resistance to interference, making it suitable for high-precision sensing applications[1]. However, its main drawback lies in the energy cost of the memory writing operation, which significantly reduces the read range and may even prevent complete data transfer under low-power excitation.

Many of the aforementioned limitations are fundamentally rooted in the constraints imposed by the current EPC Gen2 protocol architecture[10]. To overcome this structural bottleneck, future RFID-based sensing systems must undergo systematic innovations at the levels of tag structure, communication protocol, and system integration. Realizing a truly integration of sensing and communication system will require strategies that transcend the conventional tag-reader interaction paradigm.

1.1.2 Surface Acoustic Wave (SAW)

As discussed above, RFID technology, as a mature wireless communication platform, has been extensively explored for battery-less sensing applications beyond object identification and localization. Among existing approaches, the most commonly employed sensing mechanism is based on the analysis of the backscattered channel via the Received Signal Strength Indicator (RSSI)[5]. This method indirectly infers physical parameters by monitoring the amplitude variation of the tag's reflected signal. However, RSSI is a scalar and global metric whose variations are influenced not only by the measured parameters but also by several coupled factors including antenna position, tag orientation, incidence angle, and electromagnetic interference. Such multiparameter coupling results in limited robustness and ambiguity in detection, restricting the applicability of RSSI-based sensing in high-precision or tightly controlled environments[7].

To overcome these limitations, integrating RFID with other passive sensing elements has attracted growing interest. Within this context, the integration of RFID and Surface Acoustic Wave (SAW) technology has emerged as a promising solution. Unlike conventional RFID tags that rely purely on electromagnetic wave interaction, SAW devices operate based on the propagation of elastic acoustic waves along the

surface of a piezoelectric substrate[8]. This yields higher physical selectivity and stronger environmental resilience. In SAW sensors, electromagnetic energy is transmitted through backscatter or magnetic coupling, while the encoding of sensed information occurs via surface acoustic waves interacting with environmental parameters during their propagation across the substrate. Environmental changes—such as temperature, stress, and humidity—alter the propagation time, frequency response, or attenuation characteristics of the acoustic wave, which can be precisely demodulated by external SAW readers to yield quantitative sensing data under complex and harsh conditions.

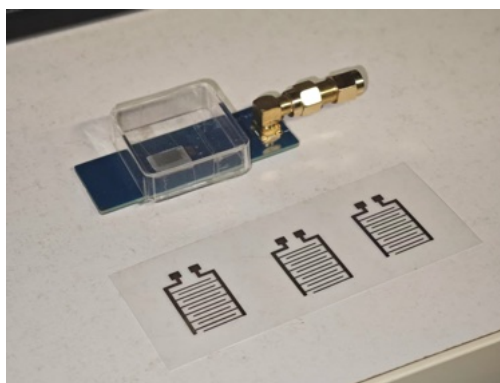


Fig 1-4 SAW Device and Masks

From a technological development perspective, SAW, as shown in Fig 1-4, is not a novel concept. Its origins trace back to the mid-20th century when it was initially utilized as a micro-electromechanical system (MEMS) component in analog signal processing. SAW elements were widely used in early television receivers and very-large-scale integration (VLSI) systems to construct reflective delay lines and resonators[7]. In the late 1970s, both academia and industry began investigating the potential of SAW devices in sensing applications, leveraging their high sensitivity to surface perturbations. Early studies focused on detecting environmental variables such as temperature, humidity, pressure, and strain. After nearly four decades of engineering refinement, SAW sensors have matured into reliable systems that exhibit high measurement accuracy not only in laboratory conditions but also in demanding

applications including automotive systems, aerospace, and industrial monitoring[8].

These developments demonstrate the multimodal sensing capabilities and sensitivity advantages of SAW devices. On one hand, various sensor configurations: such as resonator-type, delay-line-type, and filter-type, combined with tailored surface film fabrication (e.g., via deposition or sputtering) enable detection of a wide range of physical quantities. On the other hand, SAW devices exhibit stable response characteristics and strong anti-interference properties, making them well-suited for long-term deployment in harsh environments. SAW sensors are compatible with standard semiconductor microfabrication techniques, such as photolithography, sputtering, and electroplating, allowing for cost-effective, reproducible production.

Recent research has reignited interest in SAW sensors due to their passive, wireless, and miniaturized nature, which enables remote measurement without the need for power supply. With the rise of wireless communication and the growing demand for wearable electronics, the integration of SAW devices into wearable platforms has become a frontier, particularly in the context of flexible electronics.

1.2 Related Works

1.2.1 RFID Tags and Readers

With the continued maturation of RFID technology and the growing diversification of application demands, the structural forms of RFID tags have undergone significant evolution. This progression reflects not only the rapid advancement of the technology itself but also the dynamic interplay between technological development and social demands across different periods[3].

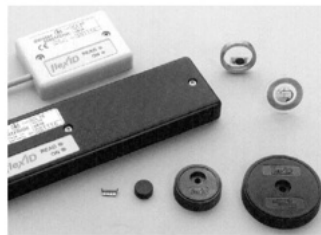


Fig 1-5 Early-stage RFID Tags[3]

In the early stages of RFID development, as shown in Fig 1-5, tags were relatively simple, often taking the form of circular or coin-shaped enclosures. These tags were primarily used for basic data storage and wireless identification. Their minimal structure and low cost made them suitable for early deployment, but their limited functionality and storage capacity increasingly became bottlenecks for more complex applications[3].

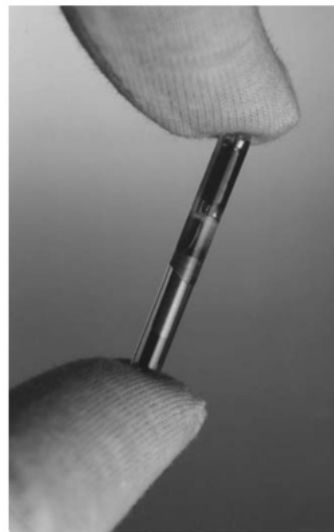


Fig 1-6 Injection-molded RFID Tag[3]

To address the demands of more specialized applications—particularly in fields such as animal identification and biomedical monitoring where biocompatibility and durability are essential— injection-molded tags, as shown in Fig 1-6, encased in glass emerged. These tags offer excellent mechanical robustness and biocompatibility, making them suitable for pet tracking, livestock management, and even human implantation in medical contexts.

With the expansion of RFID use cases across industrial, commercial, and daily environments, the structural forms of RFID tags have become increasingly diverse. For instance, plastic-encapsulated RFID tags with ruggedized integrated cases have been widely adopted in harsh industrial settings such as tool tracking and gas cylinder identification. Meanwhile, key fob-style tags have emerged as popular personal

portable solutions, commonly employed in access control systems and daily identification tasks[3].



Fig 1-7 RFID Card and Reader[3]

Since the 1990s, the development and standardization of contactless smart cards has led to the widespread adoption of ID-1 format cards (85.60 mm × 53.98 mm × 0.76 mm) as a prevalent form of RFID tag[3]. These standardized cards, as shown in Fig 1-7, are now ubiquitous in transportation, personal identification, and financial payment systems, cementing the role of RFID in consumer and authentication applications.

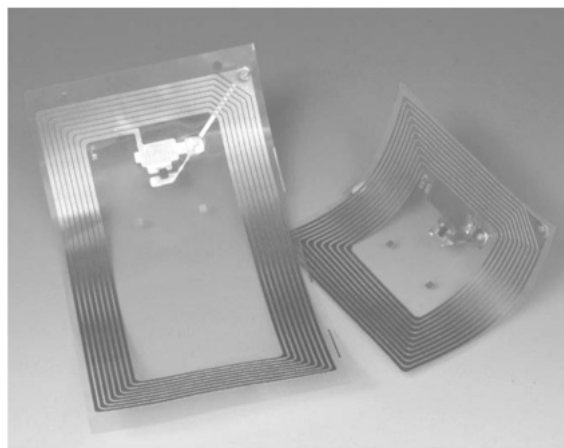


Fig 1-8 RFID Smart Labels[3]

In the 21st century, the emergence of efficient supply chain management in logistics and retail has driven the development of a new RFID form factor: the smart label, as shown in Fig 1-8, These tags are typically fabricated on flexible substrates using printed antenna technologies, resulting in ultra-thin, bendable structures that can

be easily affixed to product surfaces such as baggage tags, enabling rapid and reliable tracking throughout the supply chain.

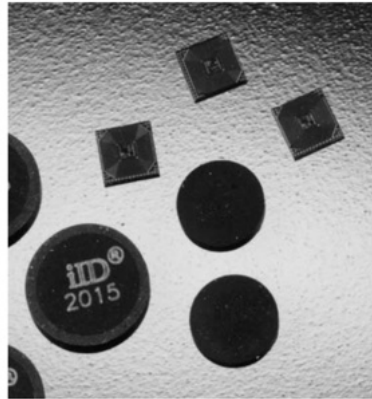


Fig 1-9 “Coil-on-chip” Tags[3]

Concurrently, advances in VLSI and antenna integration technologies have enabled the development of ultra-miniaturized “coil-on-chip” tags, as shown in Fig 1-9, in which the inductive element is directly integrated into the silicon chip. These tags feature high levels of miniaturization and integration, making them ideal for size-constrained applications such as counterfeit prevention and traceability in precision instruments and medical packaging.



Fig 1-10 RFID & Garment Industry[3]

In recent years, fueled by the rise of the Internet of Things (IoT) and wearable technologies, RFID tags have further evolved toward wearable form factors. These next-generation tags are typically manufactured using lightweight, flexible materials that allow seamless integration into textiles, garments, or skin-adhesive patches, enabling real-time monitoring of human health status and location. Smart garments, as

shown in Fig 1-10, and fabric-based electronic devices embedding RFID tags are now gaining momentum in fields such as medical diagnostics, personal health management, and sports performance monitoring.

Today, the wearable industry is becoming one of the largest application domains for RFID[5]. In particular, the garment industry has shown strong interest in RFID due to its potential to streamline logistics and enable supply chain visibility. Traditional RFID tags are often implemented using rigid substrates that are physically attached to the garment surface. However, this approach suffers from several inherent limitations, including lack of mechanical compatibility and flexibility with textile materials, and the need for additional attachment steps, which increases production complexity and cost. Such tags often fail to withstand mechanical stress and laundering conditions encountered during real-world garment usage.



Fig 1-11 A Wearable RFID Tag

Recently, both academia and industry have turned their attention to fabric-based flexible RFID tags. These tags, as shown in Fig 1-11, are designed to be directly integrated into the fabric structure, thus offering enhanced compatibility, durability, and comfort in wearable applications. Despite their significant potential, fabric-based RFID

tags still face major technical challenges in practical deployment. Among the most critical issues are the integration of RFID chips with flexible radiating elements and the design of wearable antenna systems capable of maintaining performance under mechanical deformation.

From the perspective of chip-to-textile integration, current research has yet to deliver a mature, efficient, and textile-compatible solution that aligns with conventional fabric manufacturing workflows. The current approach typically involves mounting the RFID chip onto a rigid substrate, as shown in Fig 1-12, which is subsequently attached to the textile. However, this must introduce bulky rigidity, severely compromising the fabric's flexibility and overall wearing comfort[4].

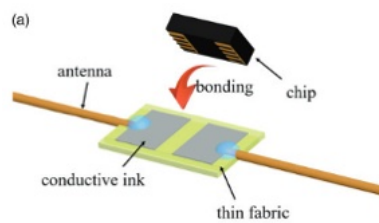


Fig 1-12 An RFID Chip on a Rigid Substrate[4]

Another widely adopted technique is the use of pre-packaged chip modules, as shown in Fig 1-13. While this approach simplifies the manufacturing process to some extent, the resulting encapsulated chip units tend to exhibit increased bulk and rigidity, further enlarging the inflexible region within the textile. Such structural rigidity hinders integration with standard weaving and knitting processes, thereby restricting the large-scale applicability of RFID fabric tags in wearable systems[4].

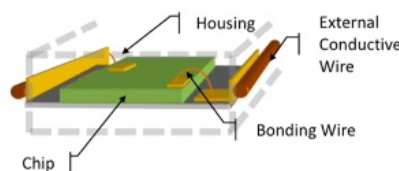


Fig 1-13 A Pre-packaged RFID Chip[4]

Recently, yarn-level chip integration technology: Primo 1D's E-Thread, as shown in Fig 1-14, process have attracted significant attention[4].

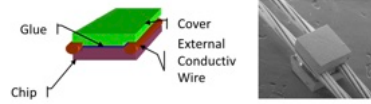


Fig 1-14 E-Thread of Primo 1D

This method uses wafer-level, as shown in Fig 1-15, semiconductor fabrication. Metallic micro-bumps are deposited onto bonding pads on an active wafer, and through precise wafer bonding and anisotropic plasma dry etching, conductive fibers are embedded into micro trenches on the wafer to establish electrical connections between the fiber and the chip.[4]

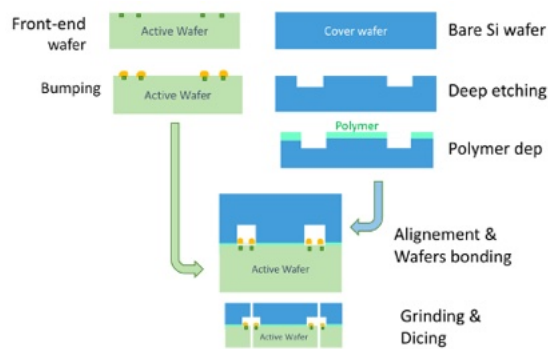


Fig 1-15 Fabrication of E-thread[4]

While this technique represents a breakthrough in chip-textile integration, it has limitations. First, the process is complex and heavily reliant on high-cost semiconductor manufacturing equipment, making it unsuitable for low-cost, large-scale production and quickly prototype in the laboratories. Second, because it necessitates modifications at the wafer fabrication level, as shown in Fig 1-16, it is incompatible with most commercially available off-the-shelf RFID chips, posing a significant barrier to practical deployment[4].

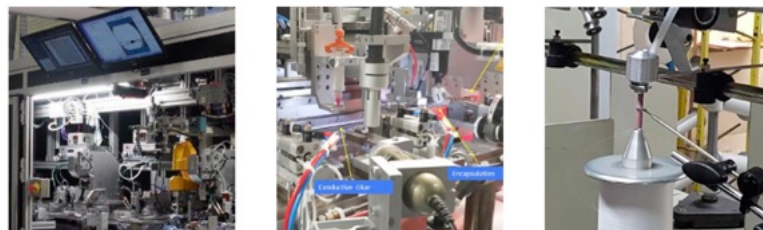


Fig 1-16 Fabrication of E-thread (Cont.) [4]

From an antenna design standpoint, the one-dimensional trench configuration required in this process occupies all four bonding pads of the chip and disables one diagonal pair. This constraint prevents the implementation of orthogonal polarization antennas, severely limiting the design flexibility and polarization diversity of the integrated RFID tag.

On the other hand, wearable RFID antenna design faces several persistent challenges. Two commonly used methods are conductive ink printing and embroidered conductive yarns. Conductive inks like silver nanoparticles, carbon nanotubes, or graphene, are applied using screen printing or inkjet deposition, as shown in Fig 1-17, to transfer antenna patterns onto fabric substrates[5].

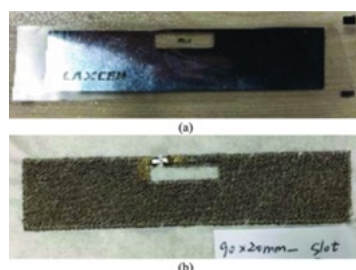


Fig 1-17 Wearable RFID Tags[5]

Alternatively, embroidery techniques employ metallic fibers or metal-coated polymer threads processed by computer-controlled embroidery machines to fabricate textile-integrated antennas. Despite the compatibility with fabric substrates, both methods result in antennas with inferior electromagnetic performance compared to traditional metallic structures. The limitations arise from the relatively poor electrical conductivity of the materials and the resolution constraints of the printing and embroidery processes, which together degrade antenna quality, reduce reading range, and impair overall RFID communication reliability, as shown in Fig 1-18.

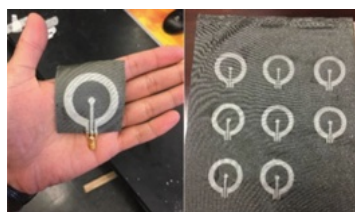


Fig 1-18 Printed Antennas[6]

Based on Primo 1D's E-Textile platform, as shown in Fig 1-18, a collaborating academic research team proposed a novel helical antenna structure. This design involves winding conductive yarn around an elastic fiber core to form a dipole antenna.

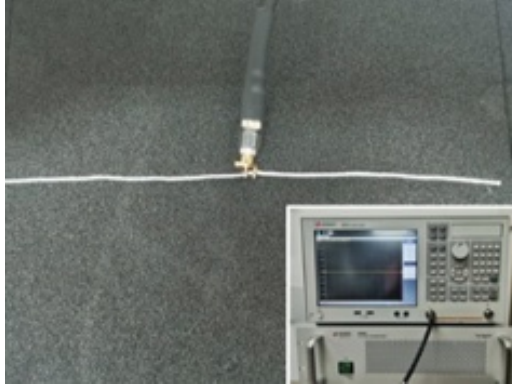


Fig 1-19 An E-Thread Dipole Antenna[6]

While the helical structure improves compatibility and flexibility within the textile matrix, it remains constrained by several fundamental issues. First, due to the relatively long wavelength associated with the UHF RFID operating band, the helical configuration struggles to achieve effective miniaturization, limiting its applicability in compact, highly integrated smart textile systems. Second, the antenna design relies only on physical length as the tunable parameter for impedance matching, resulting in minimal design flexibility. This constraint significantly complicates the optimization process, particularly when adapting the antenna to RFID chips and loads with diverse and complex impedance characteristics.[2]

A typical UHF (Ultra High Frequency) RFID system consists of three core components: a host processor or protocol controller (PC), a reader, and one or more tags. Each tag comprises an antenna and an integrated circuit (IC), with the chip's input impedance commonly represented as a complex impedance $Z_{c1} + jZ_{c2}$. Here, Z_{c1} denotes the real part of the chip impedance, equivalent to its resistive component, while Z_{c2} represents the imaginary part, which typically exhibits capacitive behavior[1].

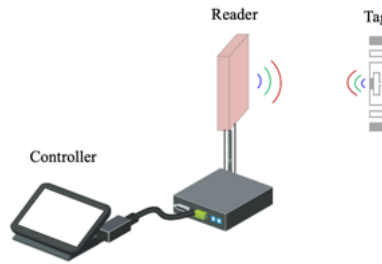


Fig 1-20 Reading an RFID Tag

The reader, as shown in Fig 1-22, transmits a continuous electromagnetic wave within a designated frequency band (e.g., 860–960 MHz) via its antenna. Upon reception by the tag antenna, a portion of the incident energy is harvested to power the tag's internal circuitry, while the remaining energy is backscattered into free space. Once activated, the tag modulates the radar cross-section (RCS) of its antenna to encode information onto the backscattered carrier signal. This modulated reflection is then received by the reader to retrieve the tag's stored data. Unlike conventional duplex wireless communication systems, RFID tags do not actively transmit electromagnetic signals; instead, data transmission and energy harvesting are achieved through passive backscatter communication.

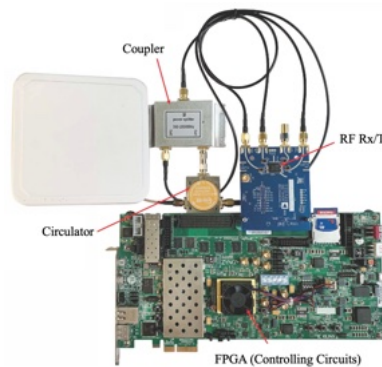


Fig 1-21 An RFID Reader[1]

In practice, each RFID tag is assigned a unique identifier and typically includes approximately 1000 bits of user memory for storing additional data or object-specific information. The RFID management system can retrieve an object's properties, location, and status by querying the tag's ID. It is worth noting that tags applied directly to

metallic surfaces often require specialized anti-metal antenna designs to maintain acceptable read ranges; otherwise, standard inlay-based antennas will exhibit severely degraded communication performance. RFID tags support standard EPC Gen2 commands such as Read, Write, Lock, and Kill, enabling flexible data handling and security control in practical applications.[1]

Of particular significance is the nature of backscatter modulation, which fundamentally differs from traditional bidirectional wireless systems. All energy in the returned signal originates from the reader; the tag merely functions as a passive reflector. The tag chip varies its load impedance to modulate the RCS of the antenna, thereby embedding stored digital information into the reflected signal. The overall communication mechanism is illustrated below. Key parameters influencing the tag's readable range include: reader transmit power, reader antenna gain, reader receiver sensitivity, tag antenna gain, tag sensitivity threshold, and the RCS of the tag antenna.

As previously discussed, current RFID readers operate in a continuous wave (CW) mode to interrogate tags. This implies that RFID-based backscatter communication systems—when considered for integration into ISAC frameworks: primarily rely on time-varying channel state information (CSI). However, due to the narrowband nature of CW excitation, such systems are inherently limited in their ability to exploit broader frequency-domain characteristics that could otherwise carry richer sensing information. This constraint presents a significant challenge for future ISAC applications seeking to harness the full spectral potential of RFID-based sensing.

1.2.2 SAW Devices

SAW devices are generally categorized into two fundamental types: resonators and reflective delay-line devices. These two device classes differ significantly in terms of operational principles and structural design that suitable for distinct application scenarios.

SAW Resonators define their resonant frequency through periodic geometrical interdigitated transducers (IDTs) fabricated on the surface of a piezoelectric substrate[7]. Environmental variations directly or indirectly influence the acoustic

propagation properties of the substrate, thereby inducing a shift in the device's resonant frequency. Consequently, the output of a resonant SAW sensor manifests as a measurable frequency change. More specifically, resonator-based SAW sensors can be further divided into single-port and dual-port configurations, as shown in Fig 1-19.

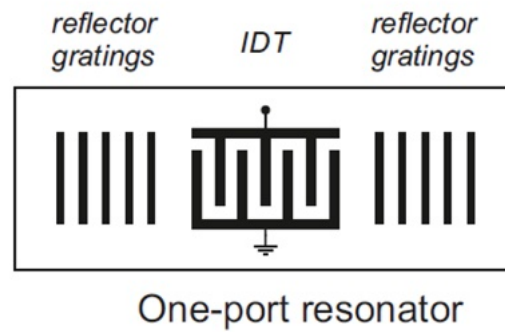


Fig 1-22 SAW Resonators[7]

A single-port resonator operates by exploiting environmental influences on the intrinsic acoustic properties of the substrate, thus enabling wireless frequency output without requiring additional circuitry, as shown in Fig 1-20.

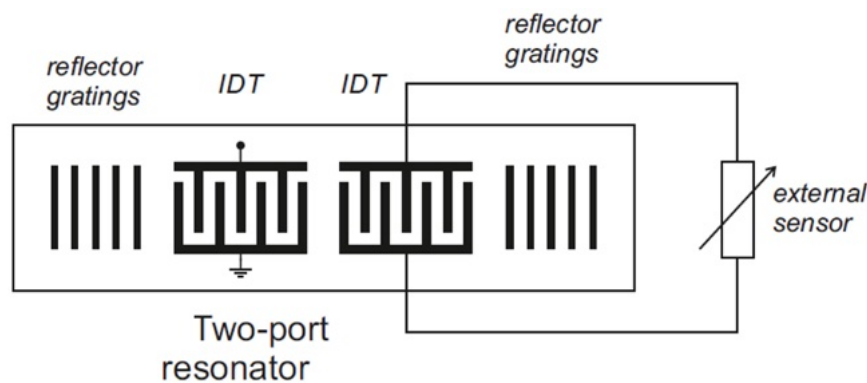


Fig 1-23 SAW Resonators (Cont.)[7]

In contrast, dual-port resonators typically work with traditional electronic sensor circuits. These circuits introduce an external electrical signal that drives the SAW structure, enabling wireless frequency-based sensing of physical parameters. Due to their low insertion loss and high frequency resolution, resonator-based SAW devices

are widely employed in high-precision sensing applications, including wireless temperature monitoring, pressure detection, and trace-level chemical or biological sensing.

Reflective delay-line SAW devices operate on the principle that acoustic waves propagate across the surface of a piezoelectric substrate at a velocity order of magnitude slower than that of electromagnetic waves—typically on the order of one millionth the speed of light. This slow propagation enables significant time delays within compact device footprints. Reflective delay-line SAW sensors also exist in both single-port and dual-port architectures, as shown in Fig 1-21.

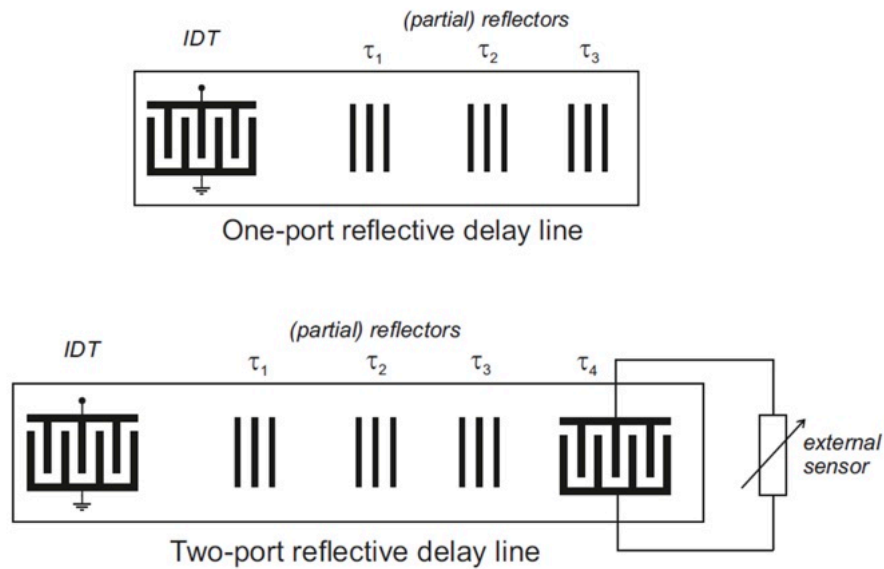


Fig 1-24 Reflective Delay-line SAW Devices[7]

These sensors can be effectively interfaced with conventional electronic sensing modules to generate specific output signals. Furthermore, owing to their inherent time-delay characteristics and time-domain signal processing capabilities, reflective delay-line SAW devices are inherently compatible with advanced modulation and multiple access schemes, such as Time Division Multiple Access (TDMA), Code Division Multiple Access (CDMA), and Orthogonal Frequency Coding (OFC). As a result, they are particularly well-suited for deployment in complex multi-user and multi-device environments.

1.3 This Work

This work proposes a novel SAW-integrated wireless sensing system based on passive RFID technology, with the aim of enabling unified sensing and communication in wearable platforms. We design a passive backscatter-based wearable RFID tag that supports both sensing and communication within an integrated framework, tailored for ISAC scenarios. This tag is specifically engineered to be compatible with commercial off-the-shelf RFID chips and SAW-based sensing components, enabling dual-functionality in a compact, energy-autonomous form factor.

To address the coupling challenges between the SAW device and the RFID chip, we develop a custom single-port resonant SAW device that conforms to the standard RFID system architecture. The device outputs sensing information through shifts in its resonance frequency, which are induced by environment. This design achieves high sensitivity and measurement precision while maintaining full compatibility with RFID backscatter communications. This could be ensuring both system scalability and high integrability. Additionally, to solve the problem of concurrent operation among multiple SAW tags, we propose a frequency-domain sampling-based reader architecture. This reader not only retains compliance with existing RFID communication protocols but also enables precise differentiation of sensing signals from multiple co-located tags through fine-grained spectral scanning and sampling. By leveraging the unique tag selection mechanism defined in the RFID protocol, the proposed system supports robust multi-sensor operation and recognition within shared electromagnetic environments.

2 RFID Tags

This study aims to develop a textile-integrated, wearable RFID tag by embedding commercially available RFID chips into conductive yarns in an efficient and scalable manner. In contrast to wafer-level fabrication methods that incur high cost and limited compatibility, our approach eliminates reliance on semiconductor processing by employing a co-design strategy across structural, electrical, and textile domains. This enables a mechanically robust and electrically stable connection between the RFID chip and conductive fiber, while preserving the inherent flexibility and wearability of the yarn. Additionally, we investigate the electromagnetic performance of various dipole antenna geometries suitable for wearable RFID tags, providing a foundational basis for the design of textile-integrated passive backscatter communication and sensing systems, as shown in Fig 2-1.[2]



Fig 2-1 RFID in a Yarn

In terms of chip integration, we propose a direct interconnection technique that bypasses wafer-level processes. The RF terminals of a commercial RFID chip are electrically bonded to a single conductive fiber, which functions both as a signal transmission line and as the radiating element of the antenna. Notably, the resulting RFID tag maintains the structural flexibility and mechanical properties of conventional yarns, making it fully compatible with standard knitting and weaving processes. This substantially lowers the barriers to adoption in smart textiles, enabling seamless integration into existing textile manufacturing ecosystems and paving the way for large-

scale deployment of flexible electronic systems.

From the perspective of electromagnetic radiation performance, we explore the behavior of wearable dipole antennas under various geometric configurations. Two antenna structures are specifically investigated: a folded dipole configuration that shortens the effective electrical length while improving impedance matching, and an inductively loaded loop structure designed to enhance magnetic coupling and broaden the operational bandwidth. Through full-wave electromagnetic simulations using HFSS, we systematically evaluate the impact of structural parameters on return loss (S11), radiation efficiency, and radiation patterns, providing quantitative design guidelines for the geometric optimization of textile-integrated RFID antennas.

Based on the proposed design methodology, we fabricated a prototype of the wearable RFID tag and conducted comprehensive performance evaluations using a standardized test platform. By comparing the measured operating frequency, reflection coefficient, antenna gain, and directivity across different structural prototypes, we demonstrate that the proposed approach maintains high mechanical flexibility while achieving stable and efficient RF performance. Compared to traditional embroidery or printed antennas, our system achieves a favorable balance between manufacturability, flexibility, and electromagnetic performance, showcasing strong potential for applications in wearable wireless communication and intelligent textile systems.[2]

2.1 Integration of RFID Chip and Wearable Radiating Element

2.1.1 Selection of Chip and Radiator

The RFID chip selected for this study is the Monza 4QT from Impinj, Inc. This chip features a compact footprint of approximately $590\text{ }\mu\text{m} \times 590\text{ }\mu\text{m}$, making it well-suited for miniaturized and highly integrated applications. The chip includes four RF interface bonding pads, with one pair of diagonal pads serving as the RF input/output ports for antenna connection, while the remaining two pads are reserved for auxiliary control functions, as shown in Fig 2-2.

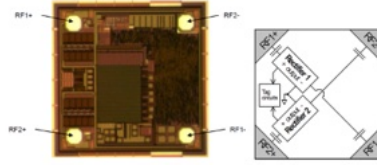


Fig 2-2 An RFID Chip

Each bonding pad has a diameter of approximately $90\text{ }\mu\text{m}$, with a center-to-center spacing of roughly $370\text{ }\mu\text{m}$. This configuration, as shown in Fig 2-3, ensures reliable bonding processability and electrical connectivity. The Monza 4QT offers high sensitivity and excellent noise immunity, and is fully compliant with the EPC Gen2 protocol, making it suitable for high-performance textile-based RFID tags operating in complex environments.

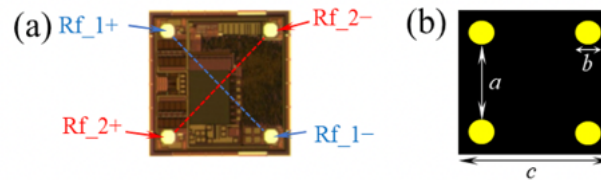


Fig 2-3 Chip Packaging

The choice of conductive fiber is critical to the overall radiation performance and robustness of the tag. Two types of conductive fibers are evaluated as single-strand radiating elements. The first is a silver-plated copper-core fiber with a diameter of approximately $80\text{ }\mu\text{m}$, offering electrical conductivity and low high-frequency loss, making it highly suitable for antenna applications. The second is a copper-core fiber coated with a polyimide (PI) insulating layer, with a diameter of approximately $50\text{ }\mu\text{m}$, as shown in Fig 2-4.

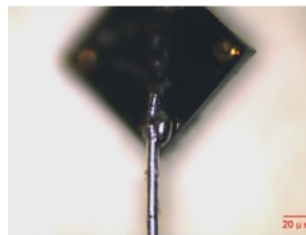


Fig 2-4 Pads on Chip

These materials not only provide superior surface insulation but also enhance thermal and mechanical durability during subsequent textile processing. As a result, the final RFID textile tag exhibits improved process compatibility and long-term reliability. Both conductive fibers retain high flexibility and wearability, effectively meeting the integration requirements for textile-embedded applications.

2.1.2 Integration Process

To ensure a reliable and efficient electrical connection between the RFID chip and the conductive fiber, this study proposes a precise and robust micro-soldering method:

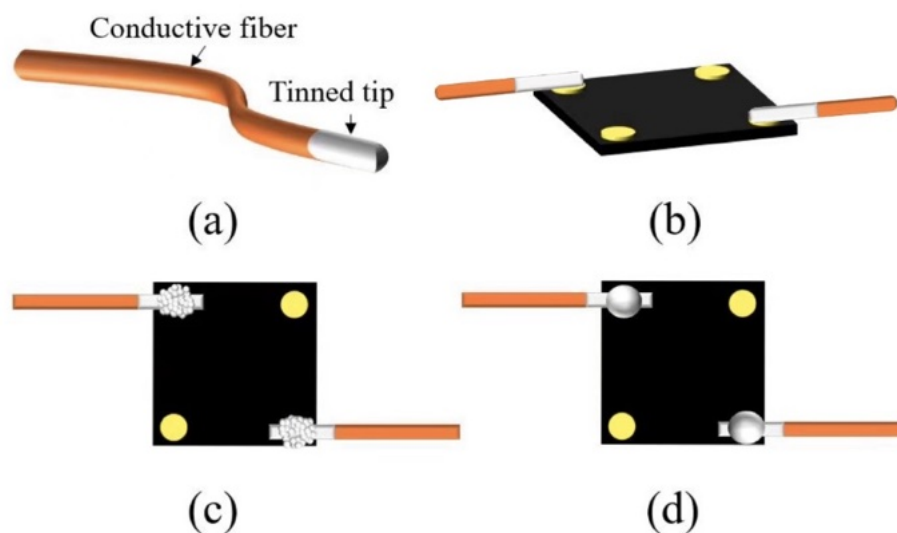


Fig 2-5 Fabrication of ID-Yarn

1. As shown in Fig 2-5 (a), The terminal section of the selected conductive fiber is immersed in molten solder. The high-temperature exposure effectively removes the insulation coating from the fiber surface, forming a uniform and dense tin-plated layer at the fiber tip. This pre-treatment significantly enhances solderability and ensures reliable subsequent bonding with the chip.
2. As shown in Fig 2-5 (b), using a micromanipulation system under optical microscopy, the pre-treated fiber tip is accurately aligned with the designated bonding pad of the RFID chip. The conductive fiber is positioned to hover

precisely above the chip pad, ensuring optimal placement for the soldering process.

3. As shown in Fig 2-5 (c), a limited amount of low-temperature solder paste is applied at the fiber–pad interface using high-precision micro dispensing equipment. This guarantees a uniform solder distribution, minimizes short-circuit risk, and prevents mechanical degradation due to excess solder volume.
4. As shown in Fig 2-5 (d), initially, a hot air gun was used to heat the bonding site. In recent works, laser soldering has been adopted to enable finer control over both temperature and duration. During this step, the solder paste melts and forms a metallurgical bond with both the pre-tinned fiber and the chip pad. Upon cooling, a stable and electrically conductive joint is established.

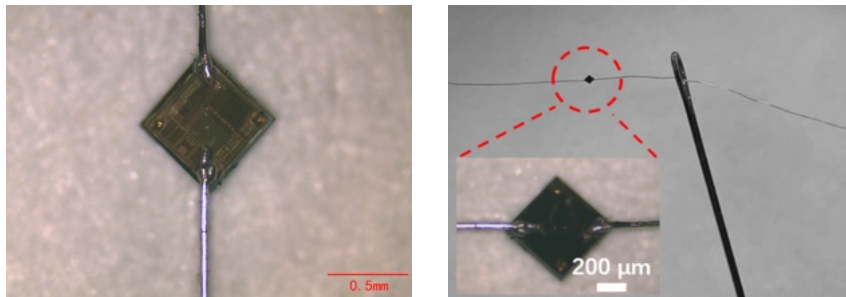


Fig 2-6 Chip Connections

2.1.3 Encapsulation and Textile Integration

To enhance mechanical robustness and provide electrical insulation at the chip–fiber structure, the entire assembly is encapsulated using black epoxy. A spin-coating process is employed to ensure uniform resin coverage, forming a well-defined ellipsoidal protective shell. The encapsulated structure is then cured at 130°C for 20 minutes to achieve full polymer cross-linking. This encapsulation safeguards the chip and solder joints against mechanical stress and environmental degradation, significantly improving operational reliability, as shown in Fig 2-7.

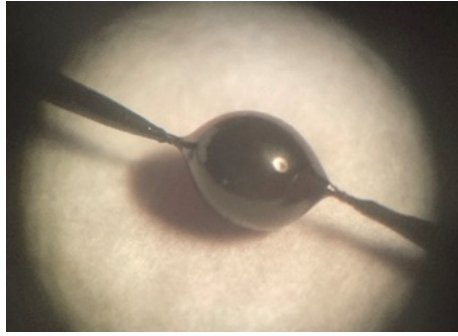


Fig 2-7 Encapsulation

Following encapsulation, the integrated chip–fiber structure is further protected through textile embedding. Specifically, a non-conductive outer fiber layer is wrapped around the encapsulated core, as shown in Fig 2-8, forming a flexible protective sheath. This final configuration results in a wearable RFID device that is fully compatible with conventional textile manufacturing processes.

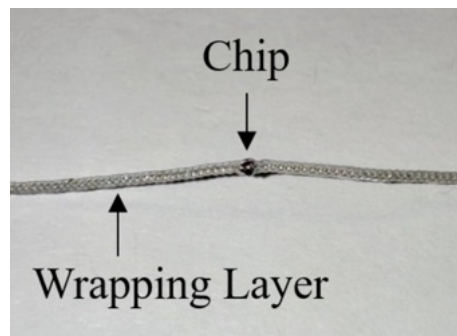


Fig 2-8 Wrapped Yarn

For laboratory-level research and prototyping, the proposed integration process offers clear advantages. It eliminates the need for complex wafer-level fabrication and avoids the constraints imposed by rigid substrates. As a result, the wearable RFID device retains mechanical properties similar to those of conventional yarns. More importantly, this fabrication strategy allows direct integration into standard weaving and knitting workflows, facilitating seamless compatibility with existing textile manufacturing infrastructure and enhancing the industrial scalability of RFID-based smart textiles.

2.2 Wearable RFID Antenna Design

In this study, the RFID antenna is constructed using a single conductive fiber serving as the radiating element. To meet practical application requirements and optimize electromagnetic performance, as shown in Fig 2-9, we propose three different antenna configurations, as illustrated below. These structures are analyzed and optimized via simulation to achieve improved impedance matching and higher power transmission efficiency.

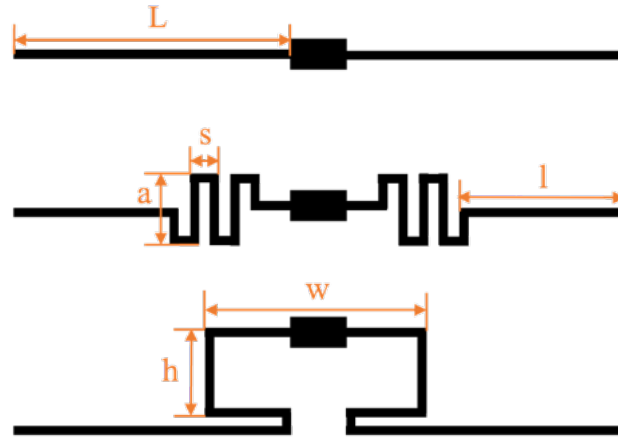


Fig 2-9 Antenna Designs

2.2.1 Dipole

The initial design is a conventional dipole antenna. As one of the most fundamental and widely used antenna types, the resonant frequency of a dipole primarily depends on the length of its arms. The length of a half-wavelength dipole antenna can be calculated by the following formula:

$$L = \frac{\lambda}{2} = \frac{c}{2f} \quad (1)$$

where L is the dipole length, λ is the wavelength of the electromagnetic wave in air, c is the speed of light (3×10^8 m/s), and f is the operating frequency. For a typical RFID operating frequency of 915 MHz, the calculated dipole length is approximately 16.3 cm.

Theoretically, a half-wavelength dipole antenna exhibits a purely resistive input

impedance of approximately 73Ω at resonance, with negligible reactance, making it highly suitable for impedance matching. However, in practical RFID applications, the chip impedance is typically capacitive. To achieve conjugate matching, the dipole length must be slightly increased so that the antenna presents an inductive reactance, compensating for the chip's capacitive characteristics. We used HFSS to model and simulate this dipole antenna. Given that the actual diameter of the conductive fiber ($\sim 60\mu m$) is much smaller than the antenna length, the model is simplified to a planar dipole.

To more accurately characterize power transfer between the chip and antenna, we define the power transmission coefficient (PTE) τ as:

$$\tau = \frac{4 \operatorname{Re}Z_{in} \operatorname{Re}Z_{chip}}{|Z_{in} + Z_{chip}|^2} \quad (2)$$

where Z_{in} is the antenna input impedance, and Z_{chip} is the chip impedance. To maximize τ , the antenna impedance should be the complex conjugate of the chip impedance. According to manufacturer data, the Monza 4QT chip's input impedance can be approximated as a parallel RC circuit with $R = 1.65\text{ k}\Omega$ and $C = 1.21\text{ pF}$. Therefore, its complex impedance is given by:

$$Z_{chip} = \frac{1}{j\omega C + \frac{1}{R}} \quad (3)$$

Using HFSS simulations, we vary the dipole length and evaluate the resulting Z_{in} to compute τ across different configurations, as shown in Fig 1-10.

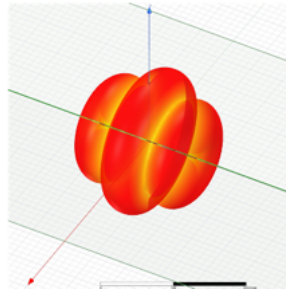


Fig 2-10 Dipole 3D Radiation

The dipole length was swept from 148 mm to 180 mm in 8 mm increments. The

simulation results are shown below, as shown in Fig 2-11.

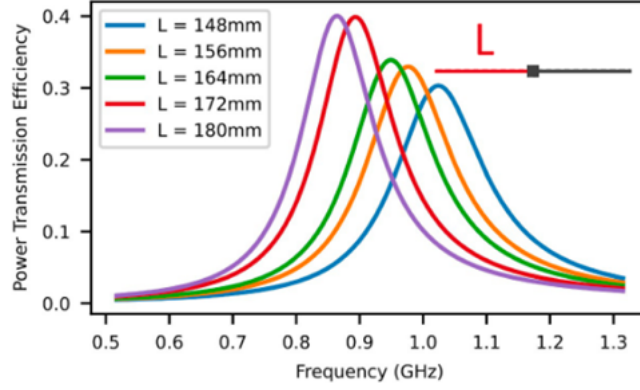


Fig 2-11 Dipole PTE

The results indicate that at the target frequency of 915 MHz, maximum power transfer occurs near a dipole length of 164 mm. However, even at this optimal length, the transmission coefficient τ remains below 40%. Further increasing the length reduces the resonance frequency but does not substantially improve power transfer. This indicates that the inductive reactance provided by a simple dipole structure is insufficient to fully compensate for the chip's capacitive impedance, leading to suboptimal matching. This motivates the need for more advanced antenna structures to enhance inductive behavior.

To account for practical wearable applications, we also evaluated antenna performance under bending conditions. The simulated power transmission efficiency of curved antennas is shown below, as shown in Fig 2-12.

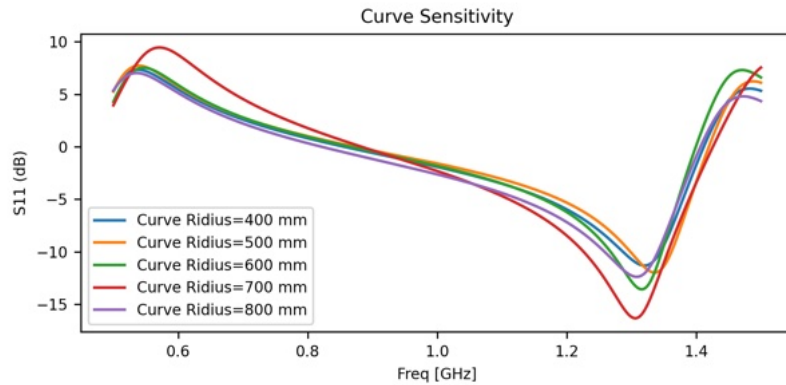


Fig 2-12 Dipole Curve Sensitivity

In these simulations, the originally planar antenna is bent to various radii. Results show no significant correlation between bending curvature and resonance characteristics in the 915 MHz band. This suggests that the proposed antenna maintains stable performance under realistic wearable deformation conditions.

Given potential variations in fiber material and geometry in practical applications, especially in fiber diameter, we further investigated the sensitivity of antenna performance to different conductive fiber diameters. HFSS simulations were conducted for diameters ranging from $w = 0.06$ mm to $w = 0.4$ mm, covering common types such as silver-coated copper, tinned copper, and PI-coated copper fibers, as shown in Fig 2-13.

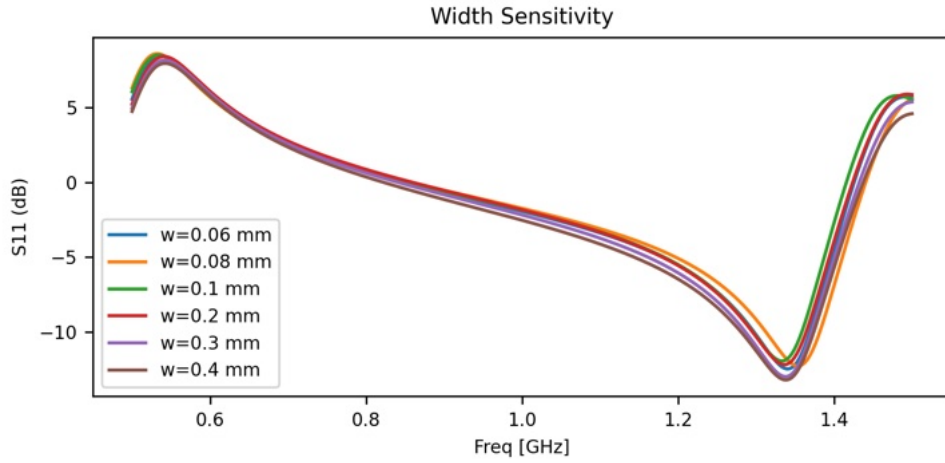


Fig 2-13 Dipole Width Sensitivity

The results indicate that, despite varying fiber diameters, the resonance frequency and reflection coefficient (S_{11}) remain largely unchanged. This confirms that the proposed antenna exhibits excellent robustness and insensitivity to variations in conductor thickness. Such robustness enhances its manufacturability using different fiber materials and production batches, ensuring tolerance to practical process variations. The proposed wearable RFID antenna design demonstrates high performance and reliability across varying bending states and conductor geometries, indicating strong feasibility for real-world, textile-integrated RFID applications.

2.2.2 Meanderline

To further improve power transmission efficiency while minimizing the physical footprint of the antenna, a meanderline structure was incorporated into the dipole antenna design. This structure introduces periodic folded segments into the antenna arms, effectively increasing the electrical path length while reducing the antenna's overall physical size. In high-frequency circuit modeling, such folded structures are commonly represented as inductive elements, which contribute positively to the antenna's reactive impedance. This inductive contribution helps counterbalance the inherently capacitive impedance of the RFID chip, thereby facilitating improved impedance matching.

As illustrated in the modeling framework, two meander segments are added symmetrically to each dipole arm. Three key geometric parameters were defined to control the shape and radiation characteristics of the meandered structure: s : spacing between meander turns (turn space), a : aperture width of the turns (turn aperture) and l : extended tail length (tail length). Using HFSS simulations, as shown in Fig 2-14, we performed parametric sweeps on each of these variables and evaluated antenna performance using the PTE τ .

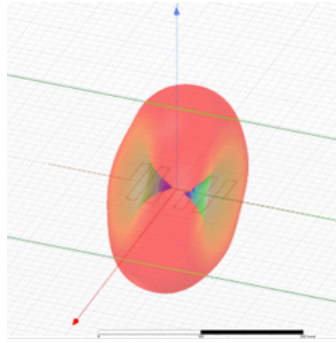


Fig 2-14 Meanderline 3D Radiation

The simulation results for s , a , and l across the 860–960 MHz RFID band are shown below. Two main resonance regions are observed, with particular emphasis on the operational range within the RFID standard band, as shown in Fig 1-15.

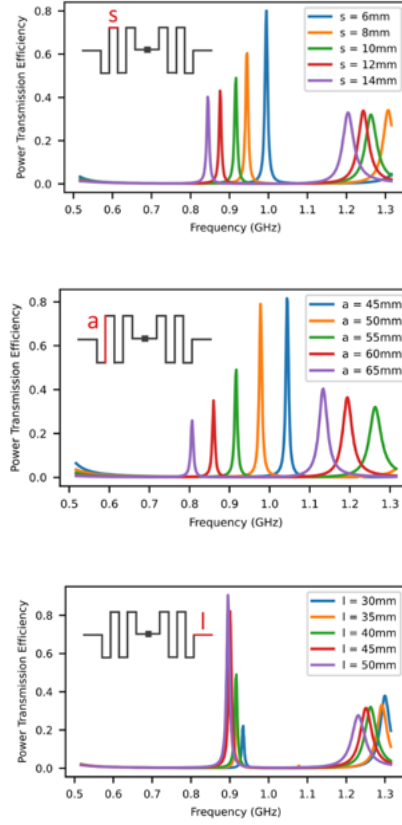


Fig 2-15 Meanderline PTE

From the frequency response analysis, it is evident that both the spacing s and aperture a significantly affect the resonance frequency. As either s or a increases, the effective electrical length of the antenna increases, shifting the resonance frequency downward. However, this shift also leads to a decline in power transmission efficiency, which can be attributed to alterations in current distribution due to extended electromagnetic coupling paths. In contrast, the tail length l has a relatively minor impact on resonance frequency but plays a noticeable role in influencing efficiency. Reducing l causes a marked drop in performance, likely because the tail acts as a supporting return path for current, thereby contributing to the antenna's overall radiation impedance.

Considering both frequency response and efficiency, the optimal parameter set was determined to be $s = 10\text{ mm}$, $a = 55\text{ mm}$, and $l = 40\text{ mm}$. Under this configuration, the antenna achieves a power transmission efficiency exceeding 50% at 915 MHz, representing a significant improvement over the conventional dipole

structure. These results demonstrate that the introduction of meanderline segments not only aids in antenna miniaturization but also enhances impedance matching with the RFID chip, providing a practical and integrable antenna solution for wearable RFID applications.

2.2.3 Inductive Loop

We further explore the integration of an inductive loop into the dipole antenna design as a means to improve impedance matching and transmission efficiency. The goal is to enhance the antenna's effective inductance to offset the capacitive impedance of the RFID chip, thereby optimizing power coupling without significantly increasing antenna length.

The inductive loop is implemented as a single-turn conductor placed centrally between the dipole arms, creating a localized magnetic field. This structure functions as an embedded inductive network, effectively increasing the inductive reactance of the antenna. Two parameters—loop width (w) and height (h)—were selected as the primary design variables. According to electromagnetic theory, the inductance of a single-turn loop can be approximated as:

$$L_{loop} \propto \mu_0 \cdot \frac{A}{l} \quad (4)$$

where A is the area enclosed by the loop, l is the loop's perimeter, and μ_0 is the permeability of free space. Thus, modifying w and h allows for precise tuning of the antenna's inductive characteristics.

We performed HFSS simulations to evaluate the antenna's performance under various combinations of w and h , focusing on resonance frequency and power transmission efficiency, as shown in Fig 2-16.

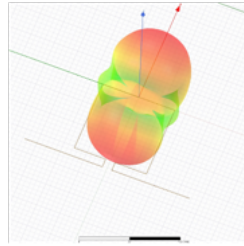


Fig 2-16 Inductive Loop 3D Radiation

The parameter ranges were set from 10 mm to 40 mm for both width and height. The resulting input impedance and power transmission performance are shown below.

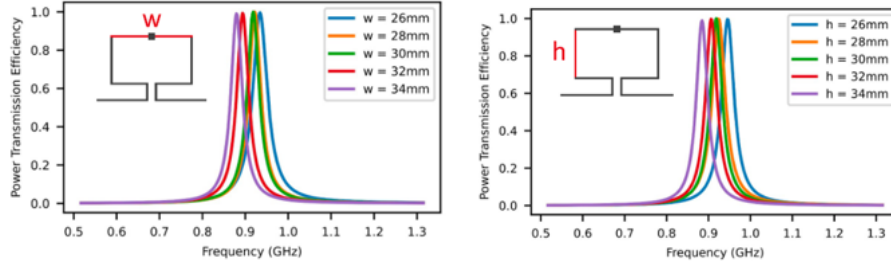


Fig 2-17 Inductive Loop PTE

Simulation results reveal that increasing either the loop width or height shifts the antenna's resonance frequency toward lower frequencies, consistent with the increase in inductive reactance. Notably, the inductive loop structure maintains relatively stable power transmission efficiency across the parameter sweep, without significant degradation. More importantly, under optimal conditions ($w = 30$ mm, $h = 30$ mm), the antenna achieves near-ideal conjugate matching with the RFID chip, with transmission efficiency approaching 100%. This represents a significant enhancement in RF energy coupling.

The inductive loop dipole substantially improves power transmission efficiency while exhibiting excellent tolerance to parameter variations. Compared to traditional structures, this design offers greater robustness against fabrication deviations, making it well-suited for integration into practical textile manufacturing workflows. By enabling local reactance tuning without requiring elongated structures, this design provides a promising path toward compact, high-performance, and fabric-compatible RFID fiber antennas.

2.3 Wearable RFID Tag Evaluation

2.3.1 Tag Prototypes

Prototype tags were fabricated and tested to validate the practical RF performance of the proposed wearable RFID tag designs

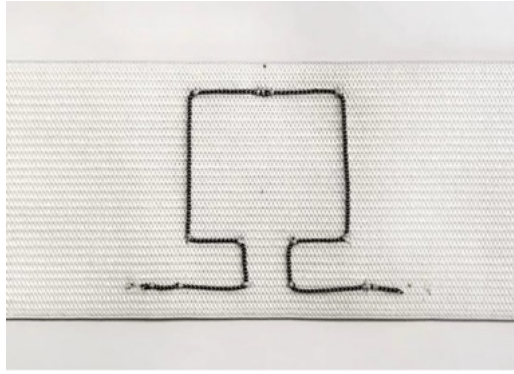


Fig 2-18 Wearable RFID Tag

It is important to note that there are differences between simulation and physical measurements. Simulations often assume ideal conductors and planar structures, neglecting practical factors such as textile geometry, fiber surface roughness, and fabrication tolerances. Therefore, simulations in this study primarily serve to guide antenna design rather than provide absolute predictions of read range. To illustrate structural differences between models and physical prototypes, the following table summarizes key parameters for each antenna configuration, as shown in Fig 2-1:

Table 2-1 Antenna Parameter

| Design | Parameters | Simulation | Actual Tag |
|-------------------------|------------|------------|------------|
| Dipole | L | 16.4 cm | 15 cm |
| Dipole with Loop | w | 30 mm | 30 mm |
| | h | 30 mm | 25 mm |
| Dipole with Meanderline | s | 10 mm | 10 mm |
| | a | 55 mm | 45 mm |
| | l | 40 mm | 40 mm |

2.3.2 Testing Platform

Read range measurements were conducted across the standard passive UHF RFID frequency band (800 MHz–1000 MHz). All tests were performed in a reflection-free anechoic chamber using the Voyantic RFID Tagformance system to ensure environmental consistency and repeatability. The reader configuration was as follows:

transmit power of 33 dBm, both transmit and receive antennas with 6 dBi gain, receive sensitivity of -70 dBm, and a frequency step size of 10 MHz, as shown in Fig 2-19.

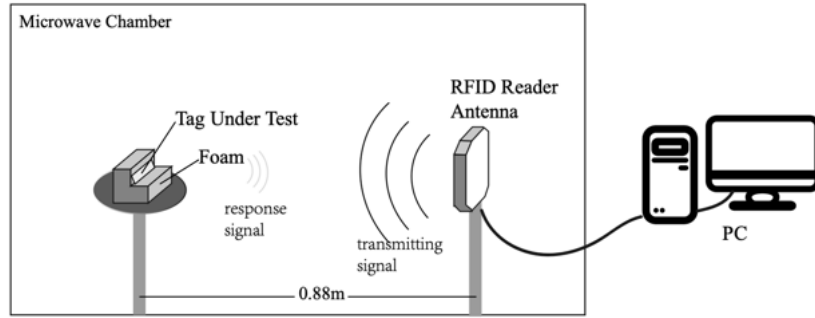


Fig 2-19 Testing Systems

2.3.3 Reading Performance

Two variants of conductive fibers (both $80\text{ }\mu\text{m}$ diameter) were used to fabricate wearable RFID tags. The read range results for all three antenna configurations are shown below, as shown in Fig 2-20.

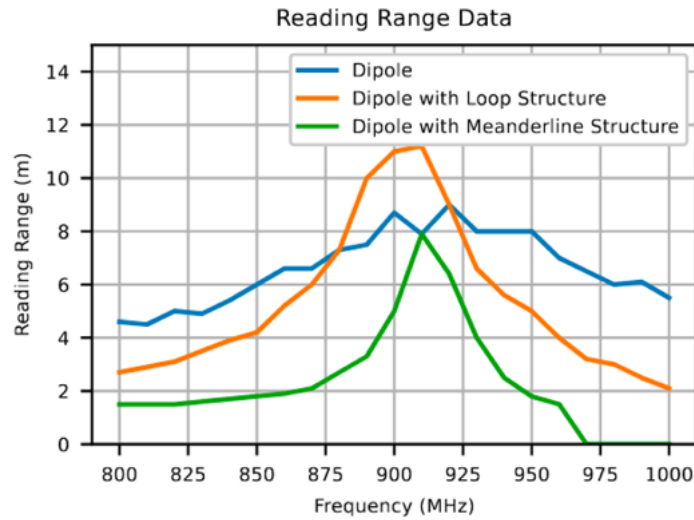


Fig 2-20 Reading Range for $80\text{ }\mu\text{m}$ Fiber

Results show that the loop-augmented dipole consistently outperforms other designs, achieving read ranges exceeding 10 meters. This aligns with the simulation results where its power transmission efficiency approached theoretical maxima. In contrast, the basic dipole antenna also demonstrated broad bandwidth and reliable read

range, confirming its practical viability. The meanderline design, however, underperformed in physical testing relative to simulations. This discrepancy is attributed to the design's high sensitivity to geometric parameters. For example, although the tail length had minimal influence on resonance frequency, it significantly affected transmission efficiency. Due to the limited precision of embroidery fabrication, controlling such parameters becomes challenging, leading to reduced performance.

Further experiments were conducted using 50 μm diameter fibers. Comparisons between fiber diameters revealed that 80 μm fibers yielded superior read performance, attributable to lower DC resistance and better high-frequency conductivity, thereby enhancing radiation efficiency and energy transmission, as shown in Fig 2-20.

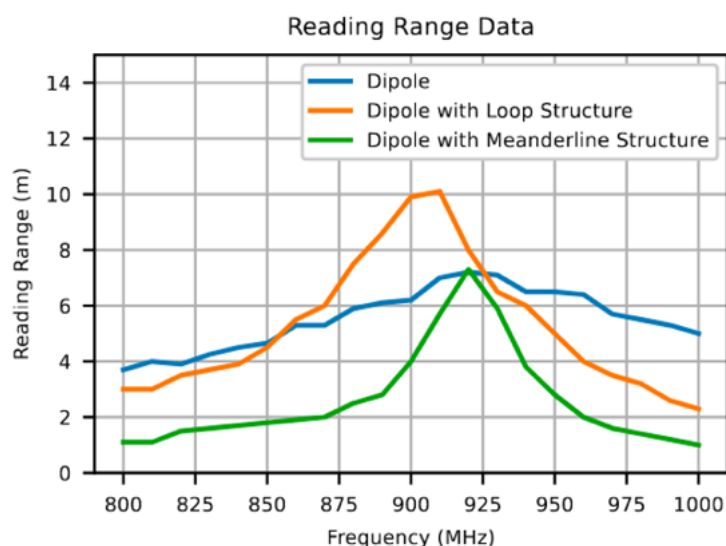


Fig 2-21 Reading Range for 50 μm Fiber

Additionally, the bandwidth performance of each antenna matched simulation trends. The basic dipole exhibited the widest bandwidth, followed by the loop design, with the meanderline showing the narrowest. This reinforces the advantage of simpler structures in terms of fabrication robustness and repeatability.

Beyond read range, the study also evaluated the Received Signal Strength Indicator (RSSI) as a metric for assessing link quality between the reader and the tag. In wearable applications, integration into fabric results in positional and structural variations due to human motion, which alters the antenna's geometry and its relative distance from the

reader—thus causing measurable RSSI fluctuations. According to the Friis transmission equation:

$$P_r = P_t G_t G_r \left(\frac{\lambda}{4\pi R} \right)^2 \quad (5)$$

where P_r is the received power, P_t is transmit power, G_t and G_r are the transmit and receive antenna gains, λ is the wavelength, and R is the distance between antennas. Clearly, bending or displacement due to joint motion dynamically alters both R and G_r , leading to time-varying P_r , observable as RSSI variation. By monitoring these fluctuations, human motion can be inferred from the time-domain waveform of RSSI—a foundational principle for passive wearable sensing.

To verify this, a wearable RFID device was placed over a subject's knee, and RSSI was recorded during flexion. The results clearly demonstrate that knee motion is reflected in corresponding RSSI changes, confirming the potential of wearable RFID tags in passive sensing via backscatter communication, as shown in Fig 2-21.

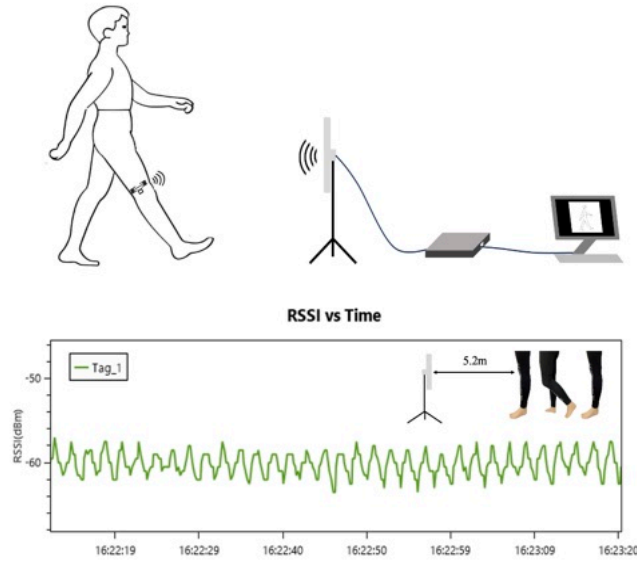


Fig 2-22 Backscatter Sensing

Based on this backscatter sensing mechanism, future work will further explore the deployment of wearable RFID tags in wireless passive sensing applications for human motion monitoring.

3 SAW-RFID System

3.1 Principles of SAW

3.1.1 Rayleigh Waves

The core mechanism of SAW devices is the Rayleigh waves. These are mechanical waves that travel along the surface of an elastic solid, exhibiting strong surface confinement due to their localized energy distribution. Rayleigh waves are characterized by two key physical properties: they are non-dispersive within a specific frequency range, meaning both phase and group velocities remain constant and independent of frequency; they travel at lower velocities than bulk acoustic waves (including longitudinal and transverse modes), with their amplitude decaying exponentially with increasing depth from the surface. These traits make Rayleigh waves exceptionally sensitive to surface perturbations, rendering SAW devices naturally well-suited for sensing applications.

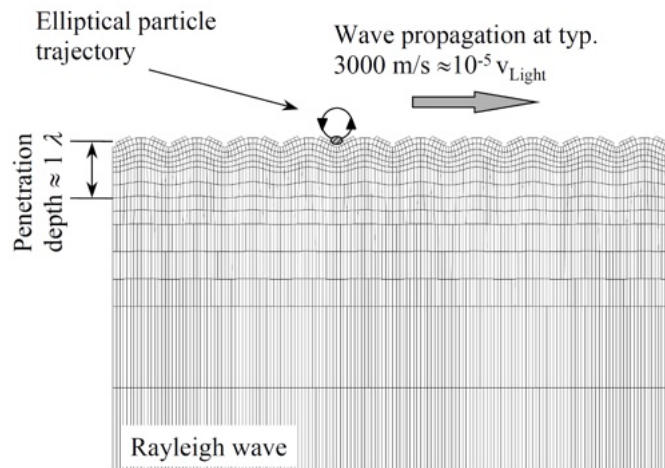


Fig 3-1 Rayleigh Waves

The particle motion in Rayleigh waves is elliptical, as shown in Fig 3-1, combining both longitudinal and transverse components. In a plane perpendicular to the direction of propagation, particles trace elliptical trajectories, either clockwise or counterclockwise, with amplitudes that decay rapidly with depth. This elliptical motion and energy localization on the surface constitute the physical foundation of SAW

behavior. As the majority of wave energy is concentrated near the surface, Rayleigh waves are highly susceptible to variations in environmental conditions such as temperature, strain, mass loading, and electric fields, making them particularly effective for use in sensitive environmental sensing applications, as shown in Fig 3-2.

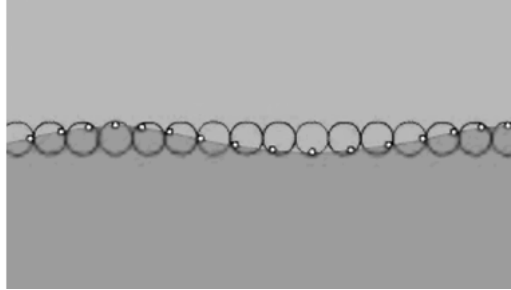


Fig 3-2 Rayleigh Waves (Cont.)

3.1.2 Interdigital Transducer (IDT)

The excitation and detection of surface acoustic waves in SAW devices are achieved through the use of IDTs, typically consisting of paired comb-like electrode structures, as illustrated below, as shown in Fig 3-3.

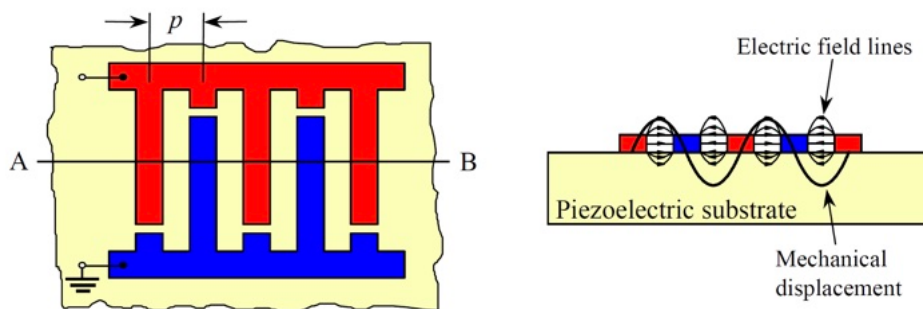


Fig 3-3 IDTs

The IDT operates on the basis of the piezoelectric effect: when an alternating voltage is applied across the electrodes deposited on the surface of a piezoelectric substrate, the induced electric field produces localized mechanical deformation, thereby exciting Rayleigh waves. Conversely, when a Rayleigh wave propagates back to the IDT, the associated mechanical strain generates a time-varying electric signal, thus completing the electro-acoustic-electro conversion cycle. The periodicity p of the IDT determines the operating frequency of the device, which satisfies the relation:

$$f = \frac{v}{p} \quad (6)$$

where f is the excitation frequency, v is the velocity of the Rayleigh wave in the substrate material, and p is the IDT pitch. Since the propagation velocity v varies across different piezoelectric materials.

3.2 SAW Fabrication

3.2.1 Piezoelectric Materials

Commonly used piezoelectric substrates for SAW device fabrication include quartz (SiO_2), lithium niobate ($LiNbO_3$), lithium tantalate ($LiTaO_3$), lead zirconate titanate (PZT), and zinc oxide (ZnO). These materials exhibit diverse characteristics in terms of acoustic wave velocity (V), electromechanical coupling coefficient (K^2), and acoustic propagation loss. A comparative summary is provided, as shown in Table 3-1:

Table 3-1 Common SAW Piezoelectric Materials

| Type | Cut | V (m/s) | K^2 (%) | Loss (dB/cm) |
|-----------|-------|-----------|-----------|--------------|
| Quartz | V-cut | 3159 | 0.22 | 0.82 |
| $LiNbO_3$ | 128Y | 3950 | 5.5 | 0.26 |
| $LiTaO_3$ | Y-cut | 3230 | 0.66 | 0.35 |
| PZT | Z-cut | 2200 | 4.3 | 2.3 |
| ZnO | X-cut | 2270 | 1.12 | 2.25 |

Among these, lithium niobate with a 128° Y-cut exhibits superior performance. Its high acoustic velocity (3950 m/s) supports higher operating frequencies for a given IDT geometry. Its large K^2 value (5.5%) enables efficient electro-acoustic conversion, while its low propagation loss (0.26 dB/cm) improves signal-to-noise ratio. Therefore, this work adopts 128° Y-cut $LiNbO_3$ as the substrate for proof-of-concept SAW device fabrication.

3.2.2 IDT Structure

The design of interdigital transducers (IDTs) involves key parameters such as

electrode width, aperture, and number of finger pairs. These factors directly influence the device's center frequency, bandwidth, and impedance matching. The following summarizes three IDT designs used in this study, as shown in Fig 3-6 and Table 3-2:

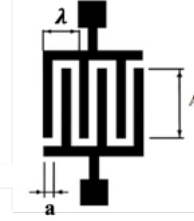


Fig 3-4 IDT Structure

Table 3-2. Design Parameters of SAW IDTs

| IDTs | Width (μm) | Aperture | Pairs |
|------|-------------------|--------------|-------|
| 01 | 3 | 120λ | 100 |
| 02 | 5 | 80λ | 60 |
| 03 | 10 | 60λ | 50 |

Here, λ denotes the acoustic wavelength, determined by the phase velocity and frequency. The electrode width controls frequency selectivity, while the aperture and number of finger pairs determine the transducer's active area and coupling efficiency. Proper selection of these parameters allows tuning the trade-offs between device sensitivity, frequency resolution, and matching characteristics.

3.2.3 Fabrication Process

The fabrication of SAW devices shares similarities with standard VLSI processing:

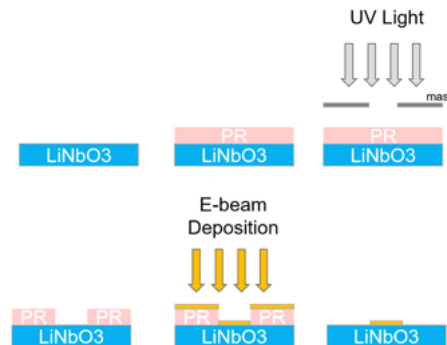


Fig 3-5 Fabrication Process

1. **Substrate Cleaning:** Using the Clean 100 wet bench, the substrate is sequentially cleaned with acetone, isopropyl alcohol (IPA), and deionized water (DI), followed by 5 minutes of ultrasonic agitation to remove surface contaminants.
2. **Photoresist Spin-Coating:** AZ5214 photoresist is applied using a Sawatec SM-180-BT spin coater—initial spin at 500 rpm for 5 seconds followed by 4000 rpm for 30 seconds—to achieve a uniform 1.5 μm film.
3. **Soft Bake:** The coated substrate is baked on a Sawatec HP-150 hotplate at 100°C for 1 minute to improve adhesion.
4. **Mask Alignment and Exposure:** Pattern transfer is performed using a SUSS MA6 mask aligner under soft contact mode to ensure precise overlay.
5. **Development:** The exposed wafer is developed in a 1:4 mixture of AZ400K and DI water for 20 seconds.
6. **DI Rinse and Dry:** The developed wafer is rinsed with DI water and dried using nitrogen gas.
7. **Gold Deposition:** A 50 nm gold layer is deposited using a Denton e-beam evaporator over a period of 3 hours.
8. **Lift-Off:** Excess photoresist and overlying metal are removed by acetone sonication on the Clean 100 platform, leaving only the patterned gold electrodes.
9. **Final Rinse and Dry:** A final DI water rinse and nitrogen drying complete the fabrication process.

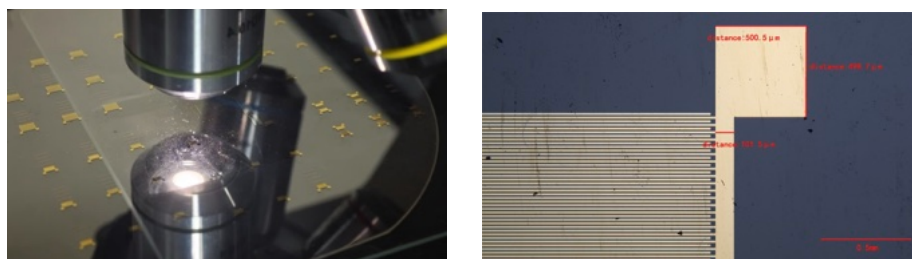


Fig 3-6 SAW Device Samples

Using this microfabrication protocol, three prototype SAW devices were successfully fabricated on LiNbO_3 substrates, as shown in Fig 3-8. The resulting gold

electrode patterns were visually uniform, with sharp edges and clean definition, confirming the structural integrity and process fidelity. These devices serve as a reliable platform for subsequent electrical and acoustic performance testing.

3.3 SAW Characterization

3.3.1 Characterization Setup

To evaluate the feasibility and sensing performance of SAW devices under different design parameters, we characterized three sets of devices fabricated with varying IDT finger widths: 10 μm , 5 μm , and 3 μm . This systematic analysis aims to assess their resonant behavior and frequency response characteristics.

To enable efficient RF characterization, we employed a vector network analyzer (VNA) for S_{11} parameter measurements and developed a custom PCB-based test fixture to simplify interconnections. Each device's two IDT terminals were either soldered or mechanically clamped to matching pads on the test PCB. The PCB was equipped with an SMA connector to ensure stable and high-fidelity signal transmission to the VNA, as shown in Fig 3-9.



Fig 3-7 Measurement Setup

3.3.2 Resonance Measurement

The VNA was configured to sweep from 100 kHz to 500 MHz with 1001 sampling points to capture fine details in the resonance behavior. The measured S_{11} data were analyzed to extract each device's resonance frequency. Fig 3-10 shows the S_{11} frequency responses for devices with different IDT finger widths:

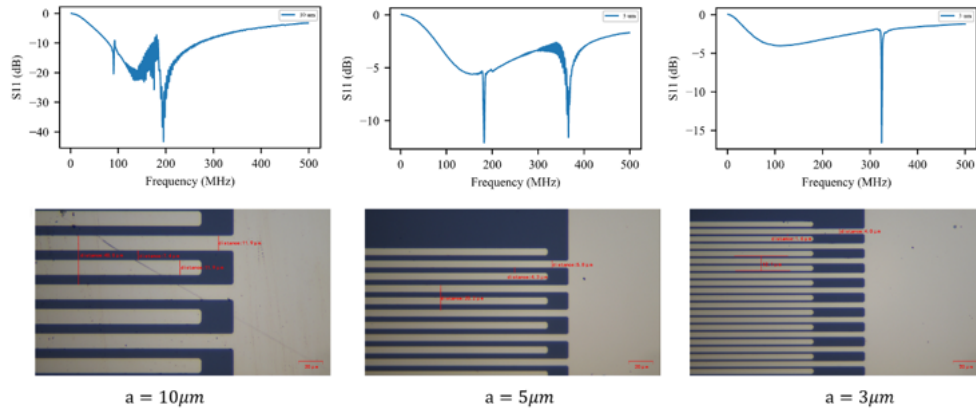


Fig 3-8 Resonate Frequency

The results clearly show that decreasing the IDT finger width increases the resonance frequency. The device with $10\mu\text{m}$ finger width exhibits a resonance peak at approximately 90.45 MHz. Reducing the width to $5\mu\text{m}$ shifts the resonance to 183.25 MHz, and further narrowing to $3\mu\text{m}$ raises the frequency to 324.38 MHz. This trend aligns with SAW theory: assuming constant electrode pitch and aperture, narrower finger widths effectively reduce the acoustic path length, thereby increasing resonance frequency.

3.3.3 Sensing Response

To assess the temperature sensitivity of the fabricated SAW devices, we performed frequency response tests under three distinct temperature conditions: room temperature (T_0), moderate heating (T_1), and elevated temperature (T_2), with T_2 limited to $\leq 100^\circ\text{C}$ to ensure thermal stability and repeatability, as shown in Fig 3-11.

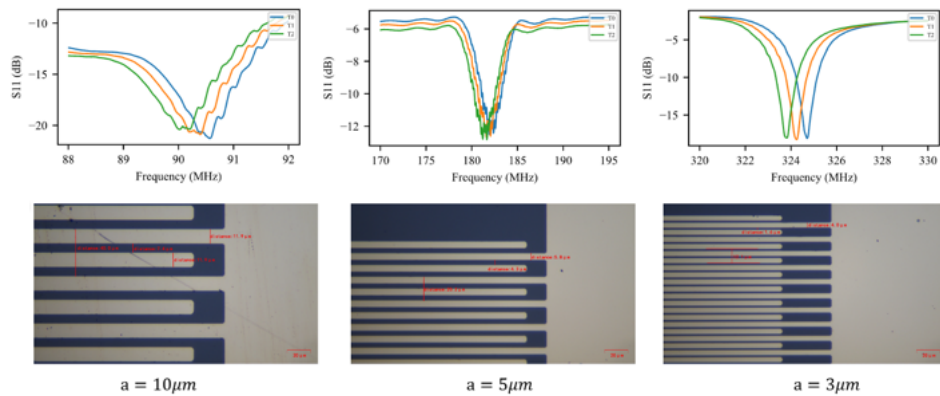


Fig 3-9 Sensing Response

During the experiment, each device was gradually heated using a hotplate or thermal chamber while continuously monitoring the S_{11} response. The main resonance frequency shift was recorded at each temperature step. The results indicate that increasing temperature consistently causes a downward shift in resonance frequency. For example, the 5 μm finger-width device exhibited a shift from 183.25 MHz at T_0 to 181.42 MHz at T_1 , and further to 178.96 MHz at T_2 .

This behavior is consistent with the underlying SAW propagation mechanism. Given that the IDT structure fixes the wavelength λ , any change in the propagation velocity v —due to thermal expansion and temperature-dependent elastic modulus that directly affects the resonance frequency f :

$$f = \frac{v}{\lambda} \quad (7)$$

As temperature increases, v decreases due to reduced stiffness and increased damping of the substrate, resulting in a lower f .

These results confirm that the fabricated SAW devices possess intrinsic temperature sensitivity. Importantly, this sensing capability operates passively and enables environmental temperature monitoring purely through spectral shifts. This demonstrates the viability of the proposed SAW structure as a foundational component in wireless, passive sensing systems.

3.4 Interrogation Principals

3.4.1 Interrogation of SAW

SAW sensors are passive elements lacking active transmission capabilities. Their operation relies entirely on external interrogation systems, as shown in Fig 3-4, for excitation and information retrieval. Based on structural design and sensing objectives, SAW sensors are typically classified into two categories: resonator-based and reflective delay-line based. Correspondingly, interrogation system architectures fall into three types: time-domain sampling, frequency-domain sampling, and hybrid approaches.

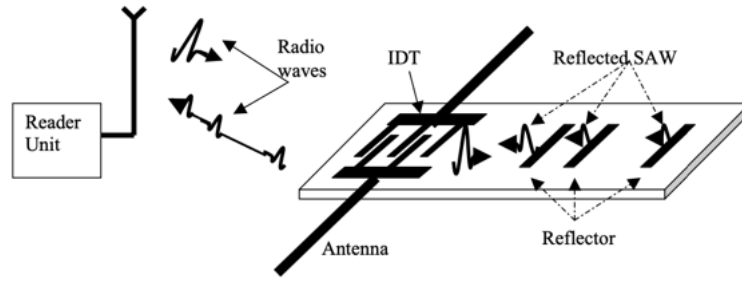


Fig 3-10 SAW Interrogation

Reflective delay-line SAW devices produce output signals comprising multiple pulses with distinct time delays, which are best analyzed using time-domain sampling architectures. Resonator-type SAW devices exhibit strong resonance responses centered at specific frequencies, making them more suitable for frequency-domain interrogation. Hybrid architectures seek to integrate the advantages of both domains to facilitate more complex multi-parameter sensing tasks, as shown in Fig 3-5.

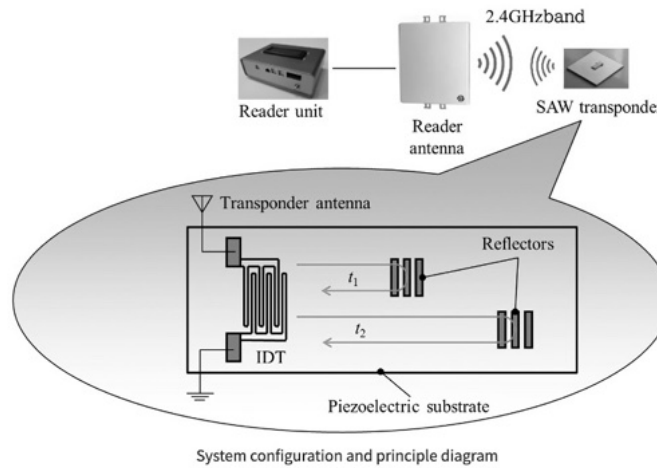


Fig 3-11 SAW Interrogation (Cont.)

In this study, to integrate SAW-based sensing with RFID communication protocols, the impedance modulation mechanism inherent to RFID systems must be considered. However, reflective delay-line SAW devices also generate multiple backscatters in the time domain, creating overlapping signals that complicate waveform demodulation and signal discrimination. Such complexity poses a significant burden on system integration and limits compatibility with RFID.

SAW resonators naturally produce narrowband absorption peaks at defined frequencies, enabling straightforward frequency-domain discrimination. Accordingly, this study adopts a single-port resonator-type SAW architecture as the core sensing unit. Impedance modulation via an RFID chip is employed to couple with the SAW device, allowing the construction of a frequency-domain mapping model for passive, spectrum-based parameter sensing.

As a core component of the SAW-based sensing system, the architecture of the SAW reader critically affects system accuracy, real-time performance, hardware cost, and application suitability. In general, existing SAW readers can be classified into two major categories: Time Domain Sampling (TDS) and Frequency Domain Sampling (FDS). These two paradigms approach signal processing from temporal and spectral perspectives, respectively, and have led to a variety of hybrid architectures in practical implementations. The following sections provide a systematic discussion of their architectural principles, signal processing strategies, and hybrid implementations.

However, a significant technical challenge in wireless multi-sensor SAW systems remains unresolved, the problem of multi-sensor discrimination in shared wireless environments. The electromagnetic waves emitted by interrogators typically have a wide beam and are uniformly distributed, leading to spatial and temporal overlaps of reflected signals from multiple SAW devices. As a result, the receiver struggles to accurately identify the origin of each signal. This overlap severely compromises measurement precision and system reliability, posing a significant challenge to the deployment of large-scale multi-sensor networks. To address this research gap, this work proposes enhanced signal coupling strategies and system-level architectural designs based on a comprehensive analysis of existing SAW reader designs.

FDS is currently the dominant interrogation scheme for SAW sensors. The core concept involves stimulating the SAW sensor with a swept-frequency excitation signal and analyzing its frequency response. The reader first generates a Frequency-Swept Continuous Wave (FSCW) using an RF signal generator. This signal is amplified and

split through a 90° hybrid coupler to form the transmitted waveform, which is filtered and then radiated via an antenna. Upon exciting the SAW sensor, the signal undergoes electromechanical conversion and is reflected back. The returned signal is amplified using a Low Noise Amplifier (LNA), mixed with the local oscillator, filtered via a Low-Pass Filter (LPF), and finally digitized by an Analog-to-Digital Converter (ADC), as shown in Fig 4-1.

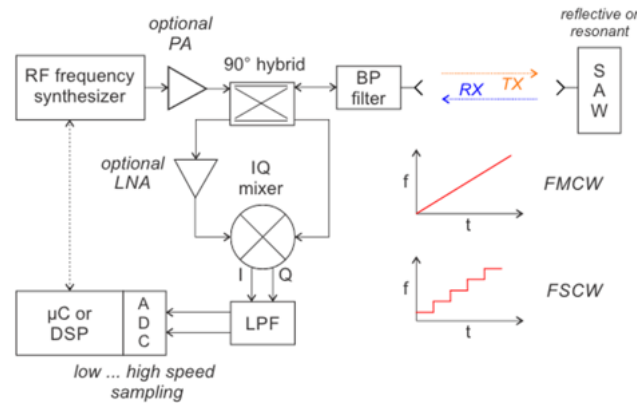


Fig 3-12 FSD SAW Reader

For SAW sensors based on reflective delay lines, multiple backscatter paths overlap to form a composite spectrum. In the frequency domain, this results in a superposition of harmonic interference components. Direct amplitude demodulation of such signals often leads to significant spectral aliasing and interference. Therefore, advanced signal processing is typically applied: zero-padding is first employed post-sampling to enhance frequency resolution; an Inverse Fast Fourier Transform (IFFT) then converts the signal to the time domain; a time-gating function is used to suppress non-target backscatters and noise; and a final FFT recovers the target resonance frequencies with improved SNR. This procedure significantly enhances the analysis of complex reflection signals and is especially suitable for multi-path environments.

SAW resonators, due to their high quality-factor (Q) and low insertion loss, exhibit pronounced spectral resonance features. FDS architectures can directly estimate the resonance frequency by sweeping the magnitude response to locate the amplitude null or phase discontinuity. Time-gated sweeping strategies further suppress out-of-band

noise and increase robustness. Moreover, to overcome the limited dynamic range in full-duplex systems, hybrid approaches such as Time-Gated FSCW (S-FSCW) are proposed. These use high-speed RF switching to temporally isolate excitation, waiting, and reception stages, achieving wide dynamic range with low sampling rate benefits.

In contrast to FDS, TDS focuses on modeling the excitation-response mechanism in the time domain, making it particularly well-suited for high-refresh-rate or low-power applications. For delay-line-based sensors, a typical TDS implementation is a pulse-radar scheme: short excitation pulses are transmitted using an SDR or pulse generator, and the temporal position and amplitude of the returning backscatters are analyzed to estimate sensor state parameters. Due to the complexity and multiplicity of backscatters, this scheme imposes stringent requirements on signal processing and ADC bandwidth. Although FDS remains predominant in commercial systems, advances in high-speed ADCs and low-power SDR platforms are expected to drive broader adoption of TDS approaches.

For resonator-type SAW sensors, which emphasize resonance rather than backscatter delay, TDS architectures continuously energize the device near its resonance frequency, allowing the cavity to form a stable acoustic response. The antenna receives a signal modulated by the SAW sensor's transfer function. The received waveform is the product of the excitation signal and the sensor's response, from which resonance information can be demodulated, as shown in Fig 4-2.

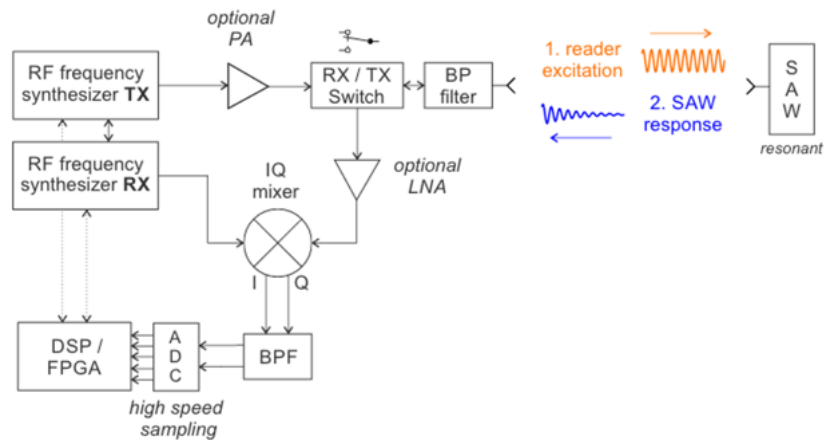


Fig 3-13 TDS SAW Reader

Several strategies exist for implementing TDS. The Direct Frequency Estimation (DFE) approach uses a traditional superheterodyne architecture, mixing the received signal with a local oscillator to generate an intermediate frequency (IF), which is then processed in the digital domain for frequency estimation. This allows frequency extraction from a single excitation, achieving extremely high refresh rates and making it suitable for dynamic monitoring. Its core relationship is:

$$f_{\text{res}} = f_{\text{IF}} + f_{\text{LO}} \quad (8)$$

where f_{res} is the resonance frequency, f_{IF} is the intermediate frequency, and f_{LO} is the local oscillator frequency. This method naturally supports Frequency Division Multiplexing (FDM), although conflict avoidance among sensors still requires distinct resonance frequencies.

The Instantaneous Frequency Measurement technique, originally developed in military microwave systems, employs six-port interferometers and delay line networks to estimate signal frequency within nanoseconds. It relies on transient interference analysis and is suited for ultra-high-speed applications, though it entails significant hardware complexity and cost. This closed-loop architecture alternately excites the SAW resonator and receives feedback signals, progressively approaching the phase minimum of the backscatter to precisely determine resonance frequency. While this enables high-precision tracking, it has a relatively low refresh rate and is more appropriate for static, high-accuracy sensing tasks.

3.4.2 Interrogation of RFID

In 2004, EPCglobal™ collaborated with major global technology companies to develop and publish the EPC™ Class 1 Gen2 air interface protocol standard, aimed at regulating the communication mechanism of UHF RFID systems operating in the 860 MHz to 960 MHz frequency band. This protocol defines the physical and logical layer interactions between the reader and the tag and has established a unified technological foundation for large-scale RFID applications such as supply chain management and logistics tracking.

Then, the International Organization for Standardization (ISO) and the

International Electrotechnical Commission (IEC) incorporated the Gen2 protocol into ISO/IEC 18000-6, adopting it as the international standard for Class C RFID communication. This standard specifies the frame format, handshake procedures, address recognition methods, and response timing control for the data exchange process. In a standard communication sequence, the reader transmits Select and Query commands. Tags in the listening state respond by entering the Reply state and returning a 16-bit random number RN16 for identification. The reader must then respond within a predefined time window with an ACK command that includes the same RN16 to complete initial authentication, as shown in Fig 4-3.

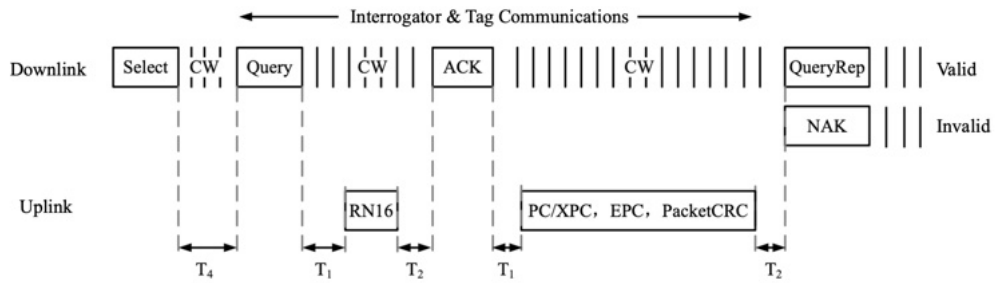


Fig 3-14 RFID Communications

When receiving a valid ACK command, the tag transmits its stored key data to the reader, including the Protocol Control (PC) bits, the Electronic Product Code (EPC), and a 16-bit CRC checksum. If the EPC is verified, the reader proceeds with further read/write or inventory operations; if invalid, the communication is terminated via a NAK command.[1]

Timing control in Gen2 is critical. T_1 represents the interval from the rising edge of the last reader command bit to the first rising edge of the tag response, reflecting response latency. T_2 spans from the last falling edge of the tag response bit to the first falling edge of the next reader command, determining the switching window in bidirectional communication. T_4 indicates the minimum inter-command gap between two consecutive reader transmissions. These timing constraints must be strictly observed during baseband module implementation to avoid timeouts and tag resets. Hence, any protocol stack implementation requires high-precision timing and state

control capabilities.

At the physical layer, uplink communication in UHF RFID systems is passive. Tags do not actively transmit energy but instead reflect the CW emitted by the reader and modulate the backscattered signal to embed information.

This study utilizes a SDR platform for coherent reception and demodulation of tag signals. Despite the presence of Carrier Frequency Offset (CFO), its impact is negligible since both transmitter and receiver share a common oscillator. The baseband model of the received signal can be expressed as:

$$y(t) = [m_{dc} + m_{mod} \cdot x(t)] \cdot e^{j2\pi\Delta f t} + n(t) \quad (9)$$

where $y(t)$ is the complex baseband signal at the receiver, m_{dc} represents the DC component due to unmodulated tag reflection, m_{mod} denotes the channel gain modulation induced by tag load switching, $x(t)$ is the baseband binary modulation sequence, Δf is the carrier frequency offset, and $n(t)$ is complex Gaussian thermal noise. This illustrates that the RFID uplink is a "passive modulation" system in which the signal power depends on reader excitation and the modulation mechanism on the tag's load switching behavior.

Gen2 specifies FM0 encoding for tag-to-reader transmissions—a form of differential encoding built upon non-return-to-zero (NRZ) logic, suited for low-power, high-reliability systems. In FM0 encoding, as shown in Fig 4-4, each bit period includes at least one signal transition. A logic 0 includes an additional mid-bit inversion, while a logic 1 maintains only the edge inversion.

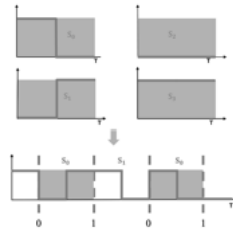


Fig 3-15 FM0 Coding

FM0 encoding is self-clocking, enabling simple timing recovery, and features distinctive signal edges that are favorable for hardware triggering. Spectrally, it avoids

DC accumulation. FM0 decoding in hardware requires accurate detection of rising and falling edges, necessitating high sampling rates and precise timing control. On SDR platforms, FM0 decoding is typically implemented using sliding window detection, phase-locked loops (PLL), and matched filtering for bitstream recovery.

3.4.3 Towards an RFID-SAW ISAC Scheme

In traditional RFID systems, the reader transmits an unmodulated CW signal to energize passive tags. Communication is achieved through electromagnetic coupling and backscatter modulation. Under the EPC Gen2 protocol, tags modulate the incident CW signal to return a standardized digital waveform, i.e., the EPC.

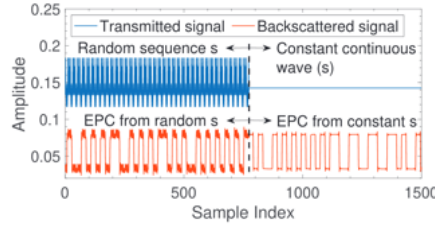


Fig 3-16 Excite RFID with Baseband Modulated Signal

However, if the CW signal is replaced with a modulated excitation such as traditional or generalized FMCW baseband signals, as shown in Fig 4-5, the returned signal may contain not only digital code but also spectral features arising from passive elements or resonant structures. This phenomenon becomes particularly relevant when SAW devices are integrated into RFID tags as sensing elements. In such a coupled system, the tag becomes both an identifier and a sensor of physical quantities.

In this architecture, the reader sends a frequency-encoded excitation signal that activates and interrogates the tag. The RF energy is received by the SAW device, exciting an acoustic wave that undergoes resonance based on the sensed physical quantity. The SAW device then modulates the backscattered signal with its resonant response, which is wirelessly transmitted back to the reader. The resulting backscatter $r(t)$ comprises both the digital ID from the RFID chip and the frequency-dependent response of the SAW resonator. The composite signal is modeled as:

$$r(t) = [m(t) + h(t)] \cdot c(t) \quad (10)$$

where $m(t)$ denotes the traditional EPC modulation, and $h(t)$ represents the frequency response of the SAW sensor. Using time-frequency analysis or an FFT, the received signal can be decomposed into:

$$R(f) = \mathcal{F}r(t) = M(f) + H(f) \quad (11)$$

Here, $M(f)$ contains discrete peaks corresponding to the digital code, while $H(f)$ comprises the spectral signature of the SAW resonances, reflecting changes in the sensed physical parameters. In this study, $m(t)$ is used to implement standard RFID reading, while $H(f)$ is decoded to retrieve sensing information.

In summary, this work aims to realize a hybrid RFID-SAW ISAC system. The RFID component provides robust digital identification, while the SAW device introduces high-sensitivity physical sensing via spectral resonance. This dual-function architecture enables the tag to act as both an ID carrier and a sensor, opening new possibilities for passive, spectrum-efficient, and cost-effective wireless sensing.

3.5 RFID-SAW Reading Framework

3.5.1 NI-LabVIEW Based SDR with FMCW

In this study, we constructed a radio frequency interrogation system based on a SDR platform. The system utilizes the NI USRP-2920 as the RF front-end, combined with the LabVIEW graphical programming environment to implement chirp signal modulation, transmission, and backscatter reception. The system, as shown in Fig 4-6 exhibits strong repeatability and modularity, laying a solid foundation for future expansions.



Fig 3-17 NI USRP-2920 Platform

Due to the limited data rate of conventional RJ45 Ethernet interfaces, which cannot

support the high-speed data transmission demands of USRP devices, and to avoid compatibility issues between different LabVIEW versions, a virtual machine was deployed on the laboratory workstation. This virtual environment runs Windows OS, with the host's physical Ethernet port mapped to the VM through network bridging. The VM is preloaded with the NI LabVIEW 2013 development suite, NI-USRP drivers, and the Modem Toolkit module, providing the necessary hardware and software support for RF signal modulation and transceiving.

Chirp signals, as a classic representation of FMCW (Frequency-Modulated Continuous Wave), are characterized by linearly increasing frequency over time in the time domain, and exhibit a flat passband response with good out-of-band attenuation in the frequency domain. This makes them highly suitable for SAW frequency response characterization and matching. A key advantage of chirp signals lies in their broadband excitation capability, which activates the full frequency-domain characteristics of SAW devices and enhances the identifiability of reflected features, as shown in Fig 4-7.

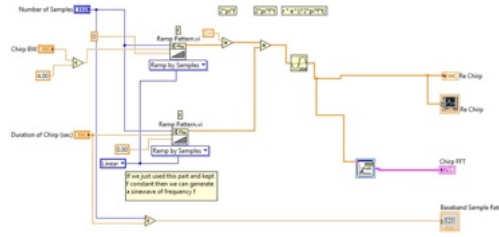


Fig 3-18 LabVIEW Sample

To enhance experimental efficiency and system reusability, a configurable chirp signal generation module was developed and encapsulated as a LabVIEW sub-VI. This module automatically reads the current USRP baseband sampling rate and generates the chirp waveform in real time based on user-defined sweep bandwidth (B) and duration (T):

$$s(t) = \cos\left(2\pi\left(f_0 t + \frac{B}{2T} t^2\right)\right), \quad 0 \leq t \leq T \quad (12)$$

where f_0 is the start frequency, B is the sweep bandwidth, and T is the sweep duration, as shown in Fig 4-8.

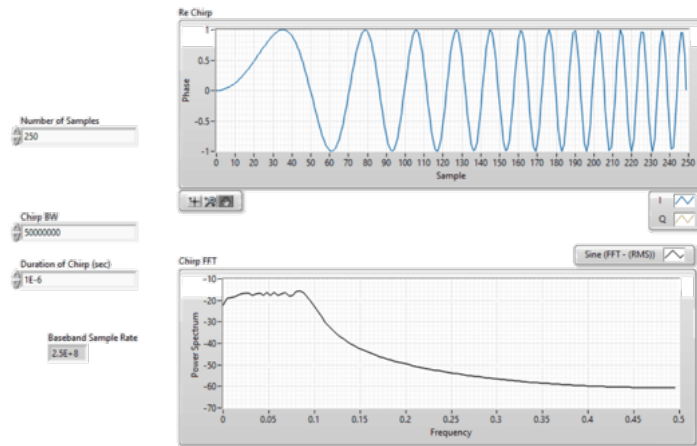


Fig 3-19 Generated FMCW Signal

To accommodate debugging and visualization, some experimental parameters were configured within the audio frequency band (20 Hz–20 kHz) and verified using a spectrum analyzer.

Experimental results confirmed that the generated chirp signal exhibited precise duration and frequency coverage. Its energy was well-centered in the frequency domain without observable distortion, indicating correctness of the generation logic. It is noteworthy that the USRP platform performs frequency translation using double-sideband amplitude modulation (DSB-AM), thus requiring the baseband chirp signal to only cover half the desired RF bandwidth to achieve complete upward frequency sweeping, as shown in Fig 4-9.

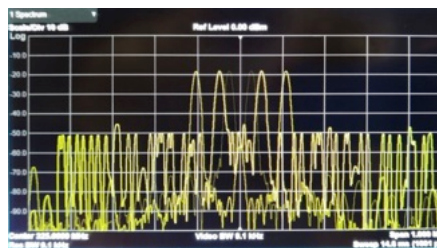


Fig 3-20 VNA Experiments

In the RF interrogation process, the system only needs to analyze absorption or notch features in the returned signal spectrum. SAW tags operate by embedding arrays of piezoelectric reflectors, which absorb specific frequencies upon excitation. This

results in frequency-selective notches observable in the backscatter spectrum. By analyzing the frequency domain response of the chirp-reflected signal, the current state of the SAW device can be inferred. This initial platform successfully implemented chirp signal baseband modulation for RFID interrogation on a USRP-based SDR reader.

3.5.2 Limitations

Despite achieving part of the system's intended functionality, the current implementation faces multiple technical bottlenecks related to refresh rate, data processing load, and compatibility with RFID standards:

Under the current architecture, each valid data point acquisition requires a complete chirp transmission and reception cycle followed by spectrum analysis. This "one sweep per read" mechanism yields a low refresh rate. In multi-tag or dynamic sensing scenarios, this severely impairs the system's responsiveness. The refresh rate R is constrained by chirp duration T and post-processing time t_{proc} :

$$R = \frac{1}{T + t_{\text{proc}}} \quad (13)$$

With T on the order of tens to hundreds of microseconds and t_{proc} affected by spectrum analysis and system overhead, the effective sampling rate can drop below 1 kHz—insufficient for high temporal resolution sensing, as shown in Fig 4-10.

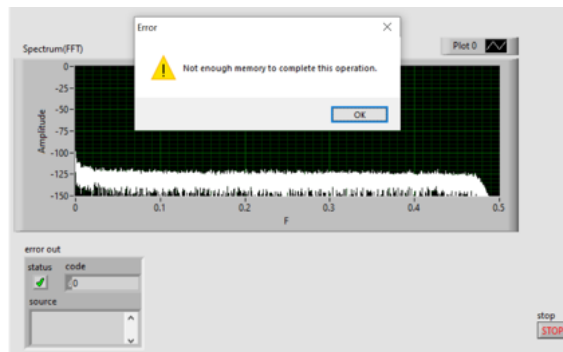


Fig 3-21 Errors in LabVIEW

Chirp signals require high-resolution sampling. For instance, a $B = 20$ MHz chirp with duration $T = 100 \mu\text{s}$ and sampling rate $f_s = 50$ MSps will produce

yielding several kilobytes per read:

$$N_{\text{samples}} = f_s \times T = 50 \times 10^6 \times 100 \times 10^{-6} = 5000 \quad (14)$$

Continuous sampling or multi-device concurrent operations would result in data volume explosion, posing substantial burdens on storage, transmission, and real-time processing. Moreover, additional steps like frequency down-conversion, windowing, and FFT are needed, posing computational challenges for embedded or mobile platforms with limited resources.

Integrating chirp-based SAW readout with existing RFID frameworks requires that each RFID communication bit period accommodates at least one chirp cycle. However, Gen2 RFID bit durations range from 25 μs (40 kbps) to 1.56 μs (640 kbps), depending on configuration. When $T \geq 20 \sim 100 \mu\text{s}$, chirp durations exceed high-data-rate bit periods, resulting in time-domain conflicts that hinder protocol synchronization. This mismatch between physical-layer timing and protocol constraints necessitates structural modifications like inserting idle slots, customizing protocol stacks, or adjusting communication timing. It will significantly increase complexity of the system.

3.5.3 GNU Radio Based SDR with OFDM

To address the limitations of the first-generation system, we developed a 2nd generation RF test platform based on the NI USRP X310 hardware and the GNU Radio open-source software toolkit. Compared to the previous USRP-2920, the X310 offers greater bandwidth, higher processing capability, and more versatile expansion interfaces, making it well-suited for high dynamic range, high SNR, and real-time SAW sensor interrogation tasks. The X310 connects to the host via dual 10 GbE SFP+ links, enabling high-speed data transmission. Its internal FPGA allows for user-defined preprocessing and signal path control, significantly enhancing real-time performance.

During setup, we first established physical connections between the host and X310 and configured static IP addressing to ensure device recognition on the local network. We then constructed the software stack on an Ubuntu-based Linux system with GNU

Radio and UHD (USRP Hardware Driver) as the development environment. GNU Radio version 3.9 and the latest stable UHD release were selected to ensure software compatibility.

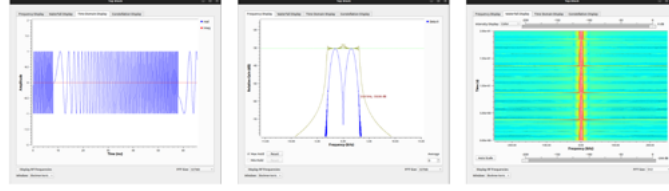


Fig 3-22 GNU Radio

Upon completing the platform setup, FMCW logic was replicated in GNU Radio. As a modular signal flow graph system, GNU Radio allows users to construct signal processing flows either graphically or via script. In this study, we used the GNU Radio Companion (GRC) interface to construct a chirp signal generation module and control the USRP X310 via UHD Sink. The transmitted chirp signal was verified via spectrum analyzer, confirming its high quality in both time and frequency domains.

As previously discussed, traditional FMCW excitation enables SAW frequency response extraction via stepwise frequency scanning. However, it suffers from structural limitations in concurrency, frequency resolution, and multi-tag decoding, making it unsuitable for high-throughput, multi-sensor applications. To overcome these limitations, we propose replacing FMCW with Orthogonal Frequency Division Multiplexing (OFDM) symbols as the baseband excitation signal, forming a new hybrid sensing-demodulation architecture that integrates SAW frequency-domain reflections with RFID digital modulation.

In this system, the transmission frequency is set between the RFID carrier and the SAW operating band, with OFDM signals modulated to create a broadband stimulus. The OFDM baseband signal is expressed as:

$$s(t) = \sum_{k=0}^{N-1} X_k \cdot e^{j2\pi f_k t}, \quad 0 \leq t < T \quad (15)$$

where X_k is the modulated symbol on the k -th subcarrier, $f_k = f_0 + k\Delta f$ denotes subcarrier frequencies, Δf is the subcarrier spacing, T is the OFDM symbol

duration, and N is the total number of subcarriers. Upon USRP transmission and SAW device reflection, the received subcarrier response is modeled as:

$$Y_k = H_{SAW}(f_k) \cdot H_{Tag}(f_k) \cdot X_k + N_k \quad (15)$$

Here, $H_{SAW}(f_k)$ denotes the SAW device response, $H_{Tag}(f_k)$ the RFID chip modulation characteristics, and N_k the noise. The system transmits a single OFDM symbol covering multiple subcarriers and retrieves frequency response information from each subcarrier via OFDM demodulation, significantly reducing sensing latency in the time domain. Simultaneously, the RFID protocol allows decoding of the tag's digital identity, achieving integrated identification and sensing.

To evaluate the feasibility and effectiveness of the proposed OFDM-based excitation scheme, we constructed an experimental platform and conducted systematic validation. The experiment focused on four key objectives: confirming basic RFID functionality via USRP, validating tag activation via OFDM symbols, observing whether tags can modulate and reflect OFDM-based signals, and analyzing returned signals to extract SAW sensing features.

We transmitted five consecutive OFDM-interrogation signals and captured the tag responses. The time-domain waveform of the received signals is shown in Fig 4-12:

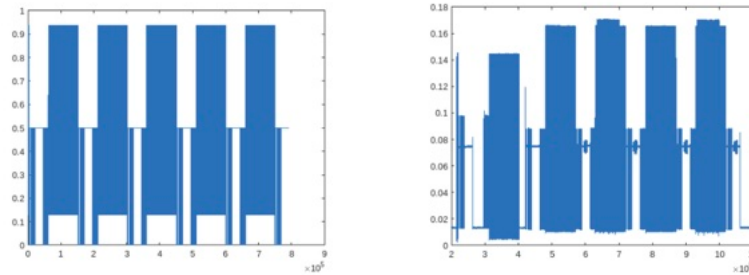


Fig 3-23 Time Domain

The responses were categorized as follows:

1. Signal transmitted, but no tag activation or response—no communication link established.
2. Tag activated and responded with an initial 16-bit random number (RN16), but baseband protocol parsing failed—communication incomplete.

3. Tag successfully activated, returned RN16, and established full bidirectional communication.

These results confirm that the USRP system supports EPC Gen2 RFID protocol, that RFID tags can be awakened using OFDM-based excitation, and that complete backscatter communication can be executed under this new waveform. More importantly, in the successfully activated cases, we observed OFDM symbol features in the tag's backscattered signal. FFT analysis of the reflected waveform yields the following spectrum in Fig 4-13:

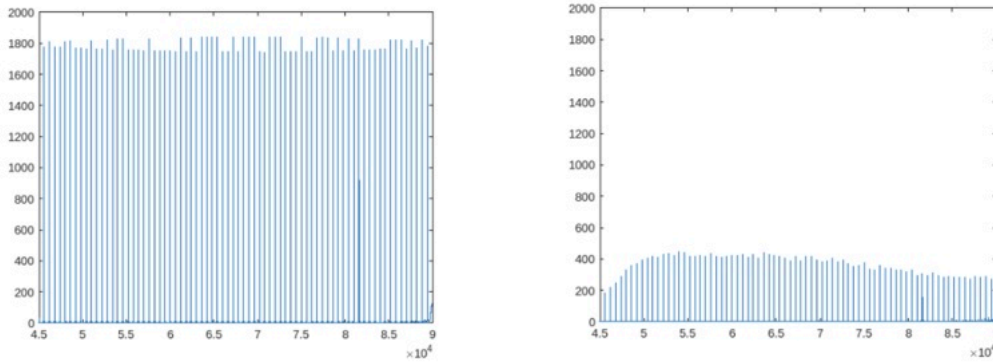


Fig 3-24 Frequency Domain

The spectrum reveals that the reflected signal contains the same subcarrier peaks as the transmitted OFDM waveform. This confirms that the OFDM symbol was backscattered by the tag and that its frequency components remained identifiable. The transmitted spectrum is flat, indicating complete coverage of the designated bandwidth. The received spectrum shows attenuation due to path loss, with discernible subcarrier structure, validating channel transmission effects. Overall, the results meet expectations and demonstrate the feasibility of OFDM-based RFID-SAW joint sensing systems.

3.5.4 Optimizations

Although the advantages demonstrated by the OFDM-based RFID-SAW joint sensing method in terms of frequency-domain demodulation efficiency and multi-tag multiplexing, practical implementation revealed severe challenges due to mutual interference between communication and sensing signals, especially with respect to

compatibility with the FM0 encoding mechanism defined in the RFID protocol, as shown in Fig 4-14.

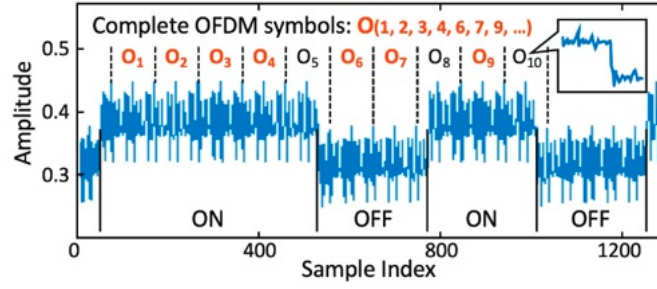


Fig 3-25 Errors in Overlapped Signals

Specifically, when the high-power OFDM baseband signal overlaps with the RFID chip's reflected EPC digital signal, the rising and falling edges are distorted by the OFDM signal's spectral content. This distortion severely compromises bit-level detection accuracy, thereby reducing EPC decoding success rates. Furthermore, because the sensing sensitivity of the SAW device is directly correlated with the excitation power of the OFDM signal, enhancing sensing performance inevitably requires stronger OFDM excitation, which in turn diminishes the communication reliability of the RFID protocol.

For sensing, any OFDM symbol coinciding with the FM0 transition region (i.e., where signal level changes occur) will suffer frequency-domain distortion, rendering the subcarrier responses unreliable. This not only degrades the stability of OFDM-based sensing but also increases system complexity, as it requires logic to detect and discard affected symbol segments, ensuring that each FM0 high or low state contains a complete, undistorted OFDM symbol.

To fill the gap, we propose an optimized demodulation scheme that integrates time-domain reference capture with frequency-domain signal compensation. As shown in the diagram, when the RFID tag receives a PIE (Pulse-Interval Encoding) excitation signal and enters the response state, its backscatter transmission has not yet begun. According to the EPC protocol, the modulation section (T1) of the returned signal does not yet carry On-Off Keying (OOK) modulation, consisting only of the tag's passive reflection

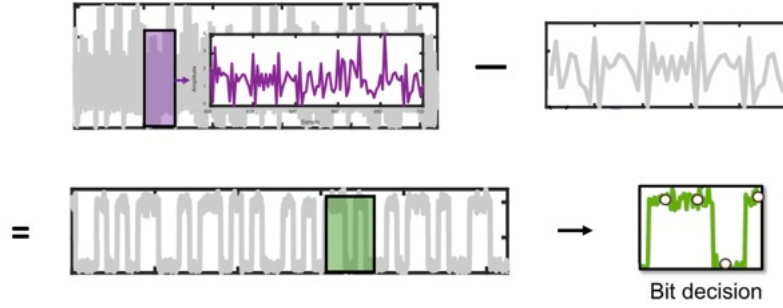


Fig 3-28 Recovery of OOK Waveforms and Bit Decisions

Simultaneously, for OFDM spectrum recovery, the T1 reference is used to estimate and compensate for the DC bias introduced by the RFID signal's amplitude modulation. Given that OOK modulation only induces amplitude shifts and minimally affects spectral content, compensating this bias restores the OFDM subcarrier structure. This approach avoids spectral corruption typically induced by FM0 transitions, eliminates the need for complex “cross-bit OFDM invalid region detection,” and preserves the integrity of each OFDM symbol, as shown in Fig 4-17.

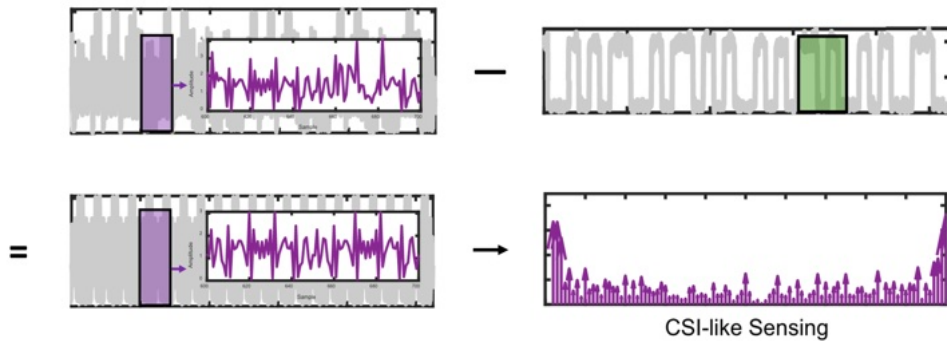


Fig 3-29 Recovery of OFDM Symbols and CSI-like Sensing

Through this optimization strategy, we effectively mitigated the destructive interference of OFDM signals on RFID EPC decoding while restoring the integrity of the OFDM waveform during communication periods. This ensures stable RFID protocol implementation alongside continuous SAW spectral sensing, balancing high-performance sensing capabilities with robust communication compatibility and improving the overall performance of the integrated OFDM Sensing and RFID Communications system.

4 Conclusion

4.1 Summary

Innovative works has been explored for the integration of SAW sensing and RFID communications. First, conventional UHF RFID chips are embedded into conductive yarns to create wearable tags. Antenna structures—dipole, meandered dipole, and inductively loop dipole—are compared, yielding a design that balances flexibility and radiation efficiency for passive SAW-readability. Second, single-port resonant SAW sensors are developed and analyzed based on piezoelectric substrates, IDTs, and reflectors. Frequency responses are validated through simulation and VNA measurements, with temperature tests confirming environmental sensitivity. Finally, an OFDM-RFID system is proposed by embedding sensing signals into EPC Gen2 protocol, enabling passive SAW interrogation with identification.

4.2 Outlook

Compared with conventional wearable sensors that rely on batteries and active RF frontends, the proposed passive backscatter sensing scheme based on RFID communication and SAW sensing offers significant advantages. First, the RFID tag's battery-free and low-profile structure enables seamless integration into textiles, greatly enhancing wearability. Second, the maintenance-free backscatter mechanism eliminates the need for battery replacement, reducing usage cost. Third, the system operates using standard RFID protocols and commercially available readers, promoting large-scale, low-cost deployment and accelerating ecosystem development. Compared to traditional RSSI-based RFID sensing systems, the integration of SAW devices enables the direct mapping of specific physical parameters, improving sensing effectiveness. This work represents a promising outlook toward realizing passive ISAC systems and establishing Body Area Networks (BANs).

For instance, a potential application scenario is in Taekwondo BANs, a sport with demanding whole-body dynamics. Monitoring flexion and force profiles is crucial for

technique assessment and injury prevention. Existing battery-powered motion sensors, although accurate, suffer from high cost, discomfort, and structural complexity. To address these issues, we propose embedding our RFID-SAW integrated system into target regions of Taekwondo uniforms and training gear. Arrays of sensors can be interrogated wirelessly by fixed readers deployed in the BANs, with SAW response data collected and processed via general computing devices. This establishes a fully passive, wireless wearable sensing BAN, as shown in Table 4-1.

Table 4-1 Comparison of Sensing Schemes

| Dimension | Traditional | RFID | This Work |
|-------------------------------------|--------------------|-------------|------------------|
| Wireless Communication | √ | √ | √ |
| Wireless Powering | | √ | √ |
| Low Component Fragility | | √ | √ |
| Low Deployment Cost | | √ | √ |
| Low Rigidity and High Comfort | | √ | √ |
| Direct Response to Physical Stimuli | | | √ |
| Low Signal Processing Complexity | | | √ |

Through the RFID-SAW integrated system, not only can real-time motion and force measurements be realized with high efficiency and minimal intrusiveness, but the system also opens a new pathway for low-cost, comfortable wearable sensing in smart sports applications. The demonstrated application in Taekwondo is only a starting point; the architecture is equally adaptable to broader domains such as medical rehabilitation, elderly care, posture evaluation, and injury prediction. The SAW-RFID wireless sensing framework is going to play a vital role in the future developments of wearable, passive, large-scale BANs and IoT systems.

Reference

- [1] 沈传魁. 面向无源智能超表面的 RFID 关键技术和相变射频开关研究[D]. 哈尔滨: 哈尔滨工业大学, 2024.
- [2] Chen T.[†], Liu Y.[†], et al. ID-Yarn: Form-factoring an RFID Tag into a Yarn and How It Can Work Well[C/OL]. (2024-12-20). [2025-05-07].
<https://ieeexplore.ieee.org/document/10965149>.
- [3] Finkenzeller K., Muller D. RFID Handbook: Fundamentals and Applications in Contactless Smart Cards, Radio Frequency Identification and Near-Field Communication[M]. Chichester: Wiley, 2010.
- [4] Bancal B. E-Thread™ technology: a Revolutionary Toolkit to Embed Electronics at the Heart of Everyday Objects[N]. Leti Innovation Days, July 3, 2018.
- [5] Liu Y., Xu L., Li Y., Ye T.T. Textile-Based Embroidery-Friendly RFID Antenna Design Techniques[C]. 2019 IEEE International Conference on RFID (RFID), Phoenix, AZ, USA, 2019: 1–6. <https://doi.org/10.1109/RFID.2019.8719270>.
- [6] Benouakta S., Hutu F.D., Duroc Y. Stretchable Textile Yarn Based on UHF RFID Helical Tag[J]. Textiles, 2021, 1(3): 547–557. <https://doi.org/10.3390/textiles1030029>.
- [7] Lurz F., Ostertag T., Scheiner B., Weigel R., Koelpin A. Reader Architectures for Wireless Surface Acoustic Wave Sensors[J]. Sensors, 2018, 18(6): 1734.
<https://doi.org/10.3390/s18061734>.
- [8] Pohl A. A Review of Wireless SAW Sensors[J]. IEEE Transactions on Ultrasonics, Ferroelectrics, and Frequency Control, 2000, 47(2): 317–332.
- [9] Kargas N., Mavromatis F., Bletsas A. Fully-Coherent Reader with Commodity SDR for Gen2 FM0 and Computational RFID[J]. IEEE Wireless Communications Letters.
- [10] Zhao C., Li Z., Ding H., Wang G., Xi W., Zhao J. RF-Wise: Pushing the Limit of RFID-Based Sensing[C]. IEEE INFOCOM 2022 – IEEE Conference on Computer Communications, 2022:

- 1–9. <https://doi.org/10.1109/INFOCOM48880.2022.9796909>.
- [11]Choi T.M., Yeung W.K., Cheng T.E., Yue X. Optimal Scheduling, Coordination, and the Value of RFID Technology in Garment Manufacturing Supply Chains[J]. IEEE Transactions on Engineering Management, 2017, 65(1): 72–84.
- [12]Luo C., Gil I., Fernández-García R. Wearable Textile UHF-RFID Sensors: A Systematic Review[J]. Materials, 2020, 13(15): 3292.
- [13]Nayak R., Singh A., Padhye R., Wang L. RFID in Textile and Clothing Manufacturing: Technology and Challenges[J]. Fashion and Textiles, 2015, 2: 1–16.
- [14]Hasni U., Piper M.E., Lundquist J., Topsakal E. Screen-Printed Fabric Antennas for Wearable Applications[J]. IEEE Open Journal of Antennas and Propagation, 2021, 2: 591–598.
- [15]Yang L., Zhang R., Staiculescu D., Wong C., Tentzeris M.M. A Novel Conformal RFID-Enabled Module Utilizing Inkjet-Printed Antennas and Carbon Nanotubes for Gas-Detection Applications[J]. IEEE Antennas and Wireless Propagation Letters, 2009, 8: 653–656.
- [16]He H., Akbari M., Sydänheimo L., Ukkonen L., Virkki J. 3D-Printed Graphene Antennas and Interconnections for Textile RFID Tags: Fabrication and Reliability Towards Humidity[J]. International Journal of Antennas and Propagation, 2017, 2017: 1–9.
- [17]Ye T.T., Yu M., Liu Y., Lau A.P.Y., Si H.T. Antennas Manufactured from Conductive Fabric Materials[M]. In: Materials in Advanced Manufacturing. CRC Press, 2022: 339–367.
- [18]Liu Y., Yu M., Xu L., Li Y., Ye T.T. Characterizations and Optimization Techniques of Embroidered RFID Antenna for Wearable Applications[J]. IEEE Journal of Radio Frequency Identification, 2020, 4(1): 38–45.
- [19]Xu L., Liu Y., Li Y., Lau P.Y., Si H., Ye T.T. Design and Fabrication of Embroidered RFID Antennas for Wearable Applications[C]. 2018 IEEE International Conference on Service Operations and Logistics, and Informatics (SOLI), 2018: 118–122.
- [20]Shi J., Liu S., Zhang L., Yang B., Shu L., Yang Y., Ren M., Wang Y., Chen J., Chen W., et al. Smart Textile-Integrated Microelectronic Systems for Wearable Applications[J]. Advanced Materials, 2020, 32(5): 1901958.
- [21]Andía G. Slenderly and Conformable Passive UHF RFID Yarn[C/OL]. 2017 IEEE International Conference on RFID (RFID): 130–136.

<https://ieeexplore.ieee.org/document/7945598>.

- [22] Rao K.S., Nikitin P.V., Lam S.F. Antenna Design for UHF RFID Tags: A Review and a Practical Application[J]. IEEE Transactions on Antennas and Propagation, 2005, 53(12): 3870–3876.
- [23] Krishnamurthy S., Bazuin B.J., Atashbar M.Z. Wireless SAW Sensors Reader: Architecture and Design[C]. 2005 IEEE International Conference on Electro Information Technology, Lincoln, NE, USA, 2005: 1–6. <https://doi.org/10.1109/EIT.2005.1626992>.
- [24] Lurz F., Ostertag T., Scheiner B., Weigel R., Koelpin A. Reader Architectures for Wireless Surface Acoustic Wave Sensors[J]. Sensors, 2018, 18(6): 1734. <https://doi.org/10.3390/s18061734>.
- [25] Pavlina J.M., Malocha D.C. A Review of Wireless SAW Sensors[J]. IEEE Transactions on Ultrasonics, Ferroelectrics, and Frequency Control, 2000, 47(2): 317–332.
- [26] Bhattacharyya R., Floerkemeier C., Sarma S. Low-Cost, Ubiquitous RFID-Tag-Antenna-Based Sensing[J]. Proceedings of the IEEE, 2010, 98(9): 1593–1600. <https://doi.org/10.1109/JPROC.2010.2051790>.
- [27] Bhattacharyya R., Floerkemeier C., Sarma S., Deavours D. RFID Tag Antenna Based Temperature Sensing in the Frequency Domain[C]. 2011 IEEE International Conference on RFID, 2011: 70–77. <https://doi.org/10.1109/RFID.2011.5764639>.
- [28] Liu S., Liu Y., Li L. The Impact of Different Proportions of Knitting Elements on the Resistive Properties of Conductive Fabrics[J]. Textile Research Journal, 2019, 89(5): 881–890. <https://doi.org/10.1177/0040517518758003>.
- [29] Reindl L., Pohl A., Scholl G., Weigel R. SAW-Based Radio Sensor Systems[J]. IEEE Sensors Journal, 2001, 1: 69–78. <https://doi.org/10.1109/JSEN.2001.923589>.
- [30] Kim Y., et al. Chip-less Wireless Electronic Skins by Remote Epitaxial Freestanding Compound Semiconductors[J]. Science, 2022, 377(6608): 859–864. <https://doi.org/10.1126/science.abn7325>.
- [31] Roh J.S., Chi Y.S., Lee J.H., Nam S., Kang T. Characterization of Embroidered Inductors[J]. Smart Materials and Structures, 2010, 19: 115020. <https://doi.org/10.1088/0964-1726/19/11/115020>.

- [32]Zuo J., Feng J., Gameiro M.G., Tian Y., Liang J., Wang Y., Ding J., He Q. RFID-Based Sensing in Smart Packaging for Food Applications: A Review[J]. *Future Foods*, 2022, 6: 100198.
- [33]Gao Y., Zhou Y., Wang J. Application Research of Logistics Tracking System Based on RFID[C]. *2007 IET Conference on Wireless, Mobile and Sensor Networks (CCWMSN)*, 2007: 853–856.
- [34]Phuyal S., Bista D., Bista R. Challenges, Opportunities and Future Directions of Smart Manufacturing: A State-of-the-Art Review[J]. *Sustainable Futures*, 2020, 2: 100023.
- [35]Makarovaite V., Hillier A.J.R., Holder S.J., Gourlay C.W., Batchelor J.C. Passive Wireless UHF RFID Antenna Label for Sensing Dielectric Properties of Aqueous and Organic Liquids[J]. *IEEE Sensors Journal*, 2019, 19(11): 4299–4307.
- [36]Khan M.S., Islam M.S., Deng H. Design of a Reconfigurable RFID Sensing Tag as a Generic Sensing Platform Toward the Future Internet of Things[J]. *IEEE Internet of Things Journal*, 2014, 1(4): 300–310.
- [37]Huang Z., Wen R., Meng J., Inserra D., Su J., Guo R., Kuang P., Li G., Wen G. Frequency Division Multiple Access Extension of Standard UHF RFID Systems for Multiple Tags Inventory with Successive Interference Cancellation[J]. *IEEE Internet of Things Journal*, 2025: 1–1.
- [38]El-Hadidy M., Khan S.I., Lasantha L., Bakri I., Tröge M., Karmakar N.C. Low-Latency Chipless RFID Tag Reader: Real-World Implementation of Frequency Hopping-Sweeping Blind Detection Technique[C]. *2024 54th European Microwave Conference (EuMC)*, 2024: 304–307.
- [39]Liu Y., Yu M., Xia B., Wang S., Wang M., Chen M., Dai S., Wang T., Ye T.T. E-Textile Battery-Less Displacement and Strain Sensor for Human Activities Tracking[J]. *IEEE Internet of Things Journal*, 2021, 8(22): 16486–16497.
- [40]Lestini F., Marrocco G., Occhiuzzi C. RFID-Based Reconfigurable Electromagnetic Devices[J]. *IEEE Journal of Radio Frequency Identification*, 2024, 8: 226–234.
- [41]Zeng Y., Liu J., Xiong J., Liu Z., Wu D., Zhang D. Exploring Multiple Antennas for Long-Range Wi-Fi Sensing[J]. *Proceedings of the ACM on Interactive, Mobile, Wearable and*

- Ubiquitous Technologies, 2022, 5(4).
- [42]Zhang Y., Han F., Yang P., Feng Y., Yan Y., Guan R. Wi-Cyclops: Room-Scale Wi-Fi Sensing System for Respiration Detection Based on Single-Antenna[J]. ACM Transactions on Sensor Networks, 2024, 20(4).
- [43]Meng K., Masouros C., Petropulu A.P., Hanzo L. Cooperative ISAC Networks: Opportunities and Challenges[J]. IEEE Wireless Communications, 2024: 1–8.
- [44]EPCglobal. EPC Radio-Frequency Identity Protocols, Class-1 Generation-2 UHF RFID Protocol for Communications at 860 MHz–960 MHz, Version 2.0.2[S]. 2021.
- [45]Zhang J., Periaswamy S.C.G., Mao S., Patton J. Standards for Passive UHF RFID[J]. GetMobile: Mobile Computing and Communications, 2020, 23(3): 10–15.
- [46]Yang C., Wang X., Mao S. RFID Tag Localization with a Sparse Tag Array[J]. IEEE Internet of Things Journal, 2022, 9(18): 16976–16989.
- [47]Shi Q., Liu L., Zhang S., Cui S. Device-Free Sensing in OFDM Cellular Network[J]. IEEE Journal on Selected Areas in Communications, 2022, 40(6): 1838–1853.
- [48] Zieliński T.P., Karpovich P., Abratkiewicz K., Maksymiuk R., Samczyński P., Duda K., Wypich M. Wireless OTFS-Based Integrated Sensing and Communication for Moving Vehicle Detection[J]. IEEE Sensors Journal, 2024, 24(5): 6573–6583.
- [49]Zhao C., Li Z., Ding H., Sun X., Xi W., Zhao J. A Self-Enhancement Solution for Standard RFIDs: Software-Based Cross-Protocol Communication and Localization[J]. Proceedings of the ACM on Interactive, Mobile, Wearable and Ubiquitous Technologies, 2024, 8(4).
- [50]Hu Z., Chen X. Localization with the Fingerprints of Multipath Angle Delay Spectrum of OFDM Signal[J]. IEEE Transactions on Wireless Communications, 2024, 23(10): 14080–14095.
- [51]Keskin M.F., Marcus C., Eriksson O., Alvarado A., Widmer J., Wymeersch H. Integrated Sensing and Communications with MIMO-OTFS: ISI/ICI Exploitation and Delay-Doppler Multiplexing[J]. IEEE Transactions on Wireless Communications, 2024, 23(8): 10229–10246.
- [52]Li Y., Wu D., Zhang J., Xu X., Xie Y., Gu T., Zhang D. Diversense: Maximizing Wi-Fi Sensing Range Leveraging Signal Diversity[J]. Proceedings of the ACM on Interactive, Mobile, Wearable and Ubiquitous Technologies, 2022, 6(2).

- [53]Luo C., Gil I., Fernández-García R. Textile UHF-RFID Antenna Embroidered on Surgical Masks for Future Textile Sensing Applications[J]. IEEE Transactions on Antennas and Propagation, 2022, 70(7): 5246–5253.
- [54]Pinapati S.P., Chen S.J., Brittain J., Caldow A., Fumeaux C. Embroidered Ground Planes for Wearable Antennas[J]. IEEE Transactions on Components, Packaging and Manufacturing Technology, 2022, 12(6): 1029–1039.
- [55]Skrobacz K., Pyt P., Jankowski-Miśkiewicz P., Węglarski M. A New Concept of Determining the RFID Chip Impedance[J]. IEEE Transactions on Microwave Theory and Techniques, 2025, 73(3): 1809–1820.
- [56]Tajin M.A.S., Amanatides C.E., Dion G., Dandekar K.R. Passive UHF RFID-Based Knitted Wearable Compression Sensor[J]. IEEE Internet of Things Journal, 2021, 8(17): 13763–13773.
- [57]Subrahmannian A., Behera S.K. Chipless RFID: A Unique Technology for Mankind[J]. IEEE Journal of Radio Frequency Identification, 2022, 6: 151–163.
- [58]Meng Z., Wu Z., Gray J. RFID-Based Object-Centric Data Management Framework for Smart Manufacturing Applications[J]. IEEE Internet of Things Journal, 2019, 6(2): 2706–2716.
- [59]Yu X., Liu J., Zhang S., Chen X., Zhang X., Chen L. Encoding-Based Range Detection in Commodity RFID Systems[C]. IEEE INFOCOM 2022 – IEEE Conference on Computer Communications, 2022: 680–689.
- [60]Zhang C., Zhang Y., Zhou J., Yuan D. VAWSS: Variational Autoencoder-Enhanced Wireless Sensing Simulator for Wi-Fi Channel State Information[C]. Companion of the 2024 ACM International Joint Conference on Pervasive and Ubiquitous Computing (UbiComp), 2024: 106–110.
- [61]De A., Datta T. UHF RFID Spectrum Detection Threshold of the Secondary User for CSI Certainty[C]. 2020 IEEE VLSI Device Circuit and System (VLSI DCS), 2020: 317–321.
- [62]Abedi A., Abari O. Can Wi-Fi Backscatter Achieve the Range of RFID? Nulling to the Rescue[C]. Proceedings of the 20th ACM Workshop on Hot Topics in Networks (HotNets), 2021: 171–177.